Study of $\eta \to e^+e^-\gamma$ Dalitz Decay to Measure the Electromagnetic Transition Form Factor of the eta meson with WASA-at-COSY Facility

THESIS SUBMITTED FOR THE DEGREE OF

Doctor of Philosophy

in

Physics

by

Ankita Goswami

Supervisor

Prof. Ankhi Roy

DISCIPLINE OF PHYSICS

INDIAN INSTITUTE OF TECHNOLOGY INDORE

INDORE - 453552, INDIA

Roll No.: 1301151001

August 2018

INDIAN INSTITUTE OF TECHNOLOGY INDORE

CANDIDATE'S DECLARATION

I hereby certify that the work which is being presented in the thesis entitled "**Study of $\eta \rightarrow e^+e^-\gamma$ Dalitz Decay to Measure the Electromagnetic Transition Form Factor of the eta meson with WASA-at-COSY Facility"** in the partial fulfillment of the requirements for the award of the degree of **DOCTOR OF PHILOSOPHY** and submitted in the **DISCIPLINE OF PHYSICS, INDIAN INSTITUTE OF TECHNOLOGY INDORE**, is an authentic record of my own work carried out during the time period from **July 2013** to **August 2018** under the supervision of **Dr. Ankhi Roy**, Associate professor, Discipline of Physics, Indian Institute of Technology Indore, Indore.

The matter presented in this thesis has not been submitted by me for the award of any other degree of this or any other institute.

Signature of the student with date
(ANKITA GOSWAMI)

This is to certify that the above statement made by the candidate is correct to the best of my/our knowledge.

Signature of Thesis Supervisor with date
(Dr. ANKHI ROY)

ANKITA GOSWAMI has successfully given her Ph.D. Oral Examination held on

---

Signature of Chairperson (OEB) Signature of External Examiner Signature of Thesis Supervisor(s)
Date: Date: Date:

Signature of PSPC Member #1 Signature of PSPC Member #2 Signature of Convener, DPGC
Date: Date: Date:

Signature of Head of Discipline
Date:

Dedicated

to

My Grandfather

Acknowledgements

I would like to acknowledge all those people who have contributed in some way to complete this dissertation. First of all, I would like to express my sincere gratitude to my advisor Dr. Ankhi Roy for the continuous support during my Ph.D. and related research, for her patience, motivation, and immense knowledge. Her guidance helped me in all the time of research and writing of this thesis. I would also like to acknowledge Dr.Susan Schadmand, my unofficial supervisor, for her guidance throughout my Ph.D. that helped me to perform my research work more efficiently. I am extremely thankful to Prof James Ritman for his support during my visits to IKP. My deeply thanks to my PSPC members Dr. Subhendu Rakshit and Dr. Antony Vijesh for their valuable suggestions and remarks during the evaluation of my progress every year. I would like to thank COSY-FFE and IKP-Juelich for providing financial assistance which buttressed me to perform my work comfortably and to attend academic conferences to accomplish my research work. I am also thankful to the organizers of different schools/ conferences/ symposium/ workshops that I have attended during my research period, for providing me an opportunity to interact with experts of my field and present my research ideas in front of the national and international physics community. I thank all the members of WASA-at-COSY collaboration for stimulating discussions during the FIKA meetings and collaboration meetings. I gratefully acknowledge Dr. Volker Hejny and Dr.Andrzej Kupsc for their valuable suggestions during analysis. I also would like to thank Dr. Daniel Lersch and Kay Demmich for the fruitful discussions about data analysis. Special thanks to Dr. Siddhesh Sawant for the valuable suggestion and support in my work. I also thank

my fellow labmates Dr. Ajay Panwar, Sudeep Ghosh, Sudhir Rode, Sumit Kundu, Jaswant Singh and Ravinder Singh for their constant co-operation and help. I would like to thank my friends at IIT-Indore Kavita Gupta, Rupali Prajapati, Indrani Chaudhuri, Nishu Kanwa and Trina Biswas for their direct or indirect help during my stay here. I am beholden to all my friends: Payal Garg, Nupur Verma, Namrata Singh, Aischarya Brahma, Deepika Jena, Himani Bhatt, Tamalika Bhattacharya, Aradhana Singh for their love and support. Last but not least, I would like to pay high regards to my family for their constant encouragement and inspiration throughout my research work and providing me with optimism in this phase of life. My highest regards to my life-coach, my late grandfather: because I owe it all to him.

(Ankita Goswami)

Abstract

We report a study of the Dalitz decay $\eta \to e^+e^-\gamma$ to measure the transition form factor of the η meson. In this Dalitz decay, which is also known as conversion decay, the η meson decays into a photon and a lepton pair (e^+, e^-). For a point-like particle, the decay rate can be calculated within the QED framework. However, for the particle with an inner structure, the decay rate is modified at the transition vertex. The transition form factor describes this modification. The form factor is calculated by comparing the experimentally measured dilepton invariant mass spectrum with the point-like QED prediction.

The transition form factor of the η meson has been measured earlier by other experiments via $\eta \to \mu^+\mu^-\gamma$ and $\eta \to e^+e^-\gamma$ decays. These decays hold a special place as the process involves only one pseudoscalar meson (η) at transition vertex. Therefore, the form factor fully describes the structure of the η meson. Although, for the determination of the η transition form factor using the $\eta \to \mu^+\mu^-\gamma$ Dalitz decay also comes with a major shortcoming of lowering the kinematic limit to measure below $q^2 = M_{ll} = 2M_\mu$, whereas, $\eta \to e^+e^-\gamma$ Dalitz decay allows the measurement much closer to $M_{ll} = 0$ for the determination of the η transition form factor. NA60 experiment reconstructed approximately 9000 events of $\eta \to \mu^+\mu^-\gamma$ using the data taken in 2003 for In-In collisions and reported the value of $\Lambda^{-2} = (1.95 \pm 0.17_{stat} \pm 0.05_{syst})$ GeV^{-2}. In this measurement, a large statistical uncertainty is observed in the higher M_{ll} region. Later on, NA60 reported an improved preliminary result, $\Lambda^{-2} = (1.951 \pm 0.059_{stat} \pm 0.042_{syst})$ GeV^{-2} which is based on an analysis of 8×10^4 low-mass muon pairs produced in p-A collisions. The same decay channel was also studied with the Lepton-G experiment. In a measurement carried out via $\eta \to e^+e^-\gamma$ with the SND detector on the VEPP-2M collider in Novosibirsk, only 109 events were reconstructed. Another measurement was performed by A2 collaboration at MAMI-C accelerator using the combined Crystal Ball (CB) and TAPS detectors, where, 1350 of $\eta \to e^+e^-\gamma$ events were reconstructed and

the value of $\Lambda^{-2} = (1.92 \pm 0.35_{stat} \pm 0.13_{syst})$ GeV^{-2} was reported. They reported $\Lambda^{-2} = (1.95 \pm 0.15_{stat} \pm 0.10_{syst})$ GeV^{-2} (preliminary result) in 2014 with an increased statistics of 2.2×10^4 $\eta \to e^+e^-\gamma$ reconstructed events. However, they report a need for more precise measurement. This motivates us for this measurement. With large statistics data set (10^9 η mesons) of WASA-at-COSY, we expect to contribute to the result significantly. The data were acquired at the Forschungszentrum Juelich, Germany in this work. The measurement was performed using the Wide Angle Shower Apparatus (WASA), a detector setup installed at the COoler SYnchrotron (COSY) Facility. The experiment has been designed to study both the production and the decay of the light mesons in hadronic interactions. WASA is a fixed target experiment. It can detect both charged and neutral particle. The experiment has a pellet target system with a target density of 10^{15} atoms/cm^2. It helps to achieve a luminosity of $10^{32}cm^{-2}s^{-1}$. The high luminosity allows the study of rare decays of mesons. The COSY is an accelerator and storage ring, which can provide both polarized and unpolarized beams of proton and deuteron in the momentum range from 0.3 GeV/c to 3.7 GeV/c. The beam collides with the pellet target and produces new particles. These particles are detected in the WASA detector in two parts: Central Detector (CD) and Forward Detector (FD). Recoil protons in pp reactions are tagged by the forward part of the detector using the missing mass technique. The forward detector has a geometrical acceptance of 3° to 18°. The neutral and charged decay fragments ($\gamma, e^{\pm}, \pi^{\pm}$) of the produced mesons are reconstructed in the central part of the detector which has a geometrical acceptance of 20° to 169°. The central part of the detector surrounds the interaction point. The Mini Drift Chamber (MDC) in the magnetic field of the solenoid, serves to achieve the information about the momentum of the charged particles. The Scintillation Electromagnetic Calorimeter (SEC) delivers the information about energy deposited by particles. The momentum information from MDC together with the deposited energy from the SEC is used for the identification of the charged particles using the $\Delta E - P$ method. The SEC is used for the

identification of the photons as well. A large data sample of pp→ppη (10^9 η meson) has been collected in 2008, 2010 and 2012 at WASA-at-COSY experimental setup. In this study data collected in 2010 has been used. For 2010 $pp\eta$ data-set, the experiment ran for 7 weeks (at 1.4 GeV with excess beam kinetic energy of 60 MeV) and the production cross section of the reaction is $9.8 \pm 1\mu$b. The large cross-section allows studying rare decay process $\eta \rightarrow e^+e^-$ (branching ratio is less than 10^{-5}). However, it contributes a large background from multi-pion production.
First of all, a presort is performed on the raw data to reduce the analysis time. The conditions for the presort are as follows:

- Exactly two reconstructed proton tracks in the final state.
- The resultant missing mass (the difference in the invariant mass of the initial and final state protons) should be larger than 0.4 GeV/c^2.

After presort, all detector parts are calibrated. Then various kinematic conditions have been implemented on the presorted and calibrated data to identify all final state particles and to suppress the background. When proton passes through the layers of FRH, it deposits its energy (ΔE) in the layers of FRH. This information is used to identify protons using $\Delta E - \Delta E$ method and to calculate their initial kinetic energy. Two protons within a time coincidence window of $\pm$6 ns are used for further analysis. The branching ratio of the decay channels containing charged pions is approximately 27 times more than the electronic decay channels. As electronic decays are naturally suppressed in the η system, it is a challenging task to separate electrons from pions. By using the $\Delta E - P$ method, electrons are separated from pions, where P is the momentum information fron MDC and ΔE is the energy deposited in SEC. Then, the time difference between the charged track in CD and the average time of two proton tracks in the forward detector is 4 ns to 12 ns and between a photon and the average time of two proton tracks in the forward detector is -30 ns to 30 ns. The tracks registered in both MDC and SEC simultaneously participate in the analysis. In the central detector, the events with at least two charged tracks

and at least one neutral track are selected. After identifying all final state particles, the missing mass technique is used to tag the η mesons.
Then a detailed study is performed in order to identify different sources of the background. All possible background channels (both phase space and in-peak) have been simulated which are mentioned in Table 1, the third column of the table defines the secondary decays of π^0. The values of cross-section and branching ratios in the table are taken from the Particle Data Group. The channel $\eta \to \gamma\gamma$ contributes as a background if

Table 1. List of simulated background channels.

Channel	Cross-section / Branching ratio	π^0 decay
$pp \to pp\pi^0\pi^0$	324 μb	$\pi^0(e^+e^-\gamma)\pi^0(\gamma\gamma)$
$pp \to pp\pi^+\pi^-\pi^0$	4.6 μb	$\pi^0(e^+e^-\gamma)$
$pp \to pp\pi^0\pi^0\pi^0$	1.34 μb	$\pi^0(e^+e^-\gamma)\pi^0(\gamma\gamma)\pi^0(\gamma\gamma)$
$\eta \to \pi^+\pi^-\pi^0$	22.6%	-
$\eta \to \pi^+\pi^-\gamma$	4.68%	-
$\eta \to \gamma\gamma$	39%	-
$\eta \to \pi^0\pi^0\pi^0$	32%	$\pi^0(e^+e^-\gamma)\pi^0(\gamma\gamma)\pi^0(\gamma\gamma)$

one of the photons interacts with the beampipe material and converts into $e^{\pm}$ pair which is known as conversion background. Both $\eta \to \gamma\pi^+\pi^-$ and $\eta \to \pi^0\pi^+\pi^-$ channels have a similar topology to the signal channel as in both the channels there are two oppositely charged tracks and one neutral track. It is seen in the simulation that pp$\to$pp$\pi^0\pi^0$ is the main source of the background in the phase space region. and $\eta \to \gamma\gamma$ is main source of background inside the peak region. A total of 7.6% background contributes inside the peak region from the η decay channels $\eta \to \gamma\gamma$, $\eta \to \gamma\pi^+\pi^-$, and $\eta \to \pi^0\pi^+\pi^-$ inside the peak region. Following conditions are used in order to supress background:

- Total energy and momentum of the system should be conserved.
- In order to suppress the conversion background the invariant mass of e^+e^- at beam pipe is plotted as a function of the radius of e^+e^- in the x-y plane which should be near zero for dilepton pairs originating from the primary vertex.

- The background present due to discontinuous electromagnetic shower in the calorimeter caused by a particle is known as split-off. The energy deposited in the calorimeter is plotted as a function of the angle between a cluster and closest charged track and a cut influenced by simulation is applied to reject split-offs.

A 4^{th} order polynomial multiplied with the phase space of multipion production pp$\rightarrow$pp$\pi^0\pi^0$ has been used to fit the background. Total 33000 $\eta \rightarrow e^+e^-\gamma$ events have been reconstructed. However, the background is still present inside the peak region. A background-subtracted invariant mass spectrum of e^+e^- is obtained which is an experimental observable for this analysis. The transition form factor of the eta meson is determined and the slope parameter is extracted. The value of the slope parameter is $\Lambda^{-2} = 2.8 \pm .13_{stat} \pm 0.16_{syst}$ GeV^{-2}, which is related to the charge radius of the η meson. Some of the form factor bins shows fluctuations which is attributed to some unknown source of background which has yet to be understood.

The organization of the thesis is as follows:

Chapter 1 provides an introduction to the Standard Model of Particle Physics and QCD. Later on, a review of the theoretical and experimental measurements of the transition form factor of the η meson is reported.

Chapter 2 describes the WASA detector system at COoler SYnchrotron in Juelich, Germany and the details about the software tools used in the analysis.

Chapter 3 provides the detailed study of the steps to prepare the data for analysis by presorting and calibration.

Chapter 4 describes the detailed study of background and the analysis steps to obtain a clean data sample of $\eta \rightarrow e^+e^-\gamma$ channels.

Chapter 5 contains the results, summary, and conclusion of this thesis.

Contents

Figures

Tables

Chapter 1

Introduction

What are the ultimate building blocks of the matter and what are the forces that govern the interaction between them? These type of questions have perplexed the human minds. From puzzles, come the answers. From fire, water, ice and earth to the modern periodic table of elements, from an understanding of the atoms to the stars, we have made rapid progress. According to Mendlive's periodic table, matter in the universe is made up of approximately 100 elements. This implies that the matter is made up of the atoms. Nearly century ago, after the discovery of nucleus scientists realizes that atoms are not the elementary particles. Even the nucleus of an atom has proton and neutron. This was the substantial simplification in our understanding of the universe. In the middle of the 19^{th} century, many more subatomic particles were discovered. It was found that the subatomic particles like proton and neutrons are made up of quarks (up, down, bottom, top, charm and strange). In addition to quarks, there is another class of subatomic particles called leptons. Now come to the other question that what are the forces via these particles interact. There are four fundamental forces that govern the interaction among these particles. The elementary particle and the forces are discussed in the next section.

The Standard Model (SM) is one of the most successful theory in particle physics. SM is explained below in but still, there are frontiers to explore.

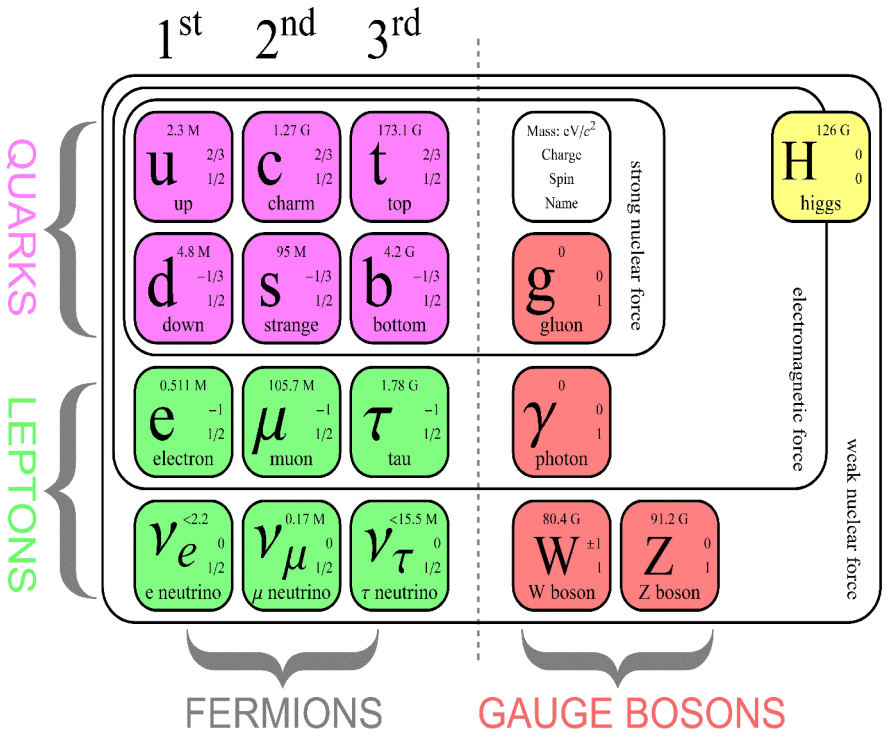

Figure 1.1. Schematic depiction of the Standard Model of elementary particles, with the three generations of matter, gauge boson in the fourth column, and the Higgs boson in the fifth [1].

1.1 Standard Model

The Standard Model encapsulates the best understanding of the fundamental particles that make up nearly everything in the universe and the interaction among them. It took a long time to build this model. In 1897, the electron was discovered by J.J. Thomson and scientists at the Large Hadron Collider found the final piece of the puzzle, the Higgs boson, in 2012 [2] [3]. The Standard Model is a well-established and a well-tested physics theory in the particle physics. There are 12 fundamental particles and five gauge bosons (force-carrying particles) in the SM. The fundamental particles occur in two primary groups called quarks and leptons having half-integral spin. Again, each group is divided into three generations according to their mass. "up (u) and down (d) quarks" are the first generation, then comes "charm (c) and strange (s)" and "top (t) and bottom (b)". Similarly leptons of first generation are "electron (e) and electron neutrino (ν_e)", second generation "muon (μ) and muon neutrino

(ν_μ)" and third generation "tau (τ) and tau neutrino (ν_τ)". Electron, muon and tau have electric charge and mass. However, neutrinos are neutral and have very little mass. There are four fundamental forces through which particles interact are strong, electromagnetic, weak and gravitational. The gravitational force is being excluded from SM as it has a negligible effect at the microscopic level. Remaining three forces work via five gauge bosons, quarks interact via gluons, γ is a force carrier of electromagnetic force and $W^{\pm}$ and Z bosons are carrier of the weak force. Also, Higgs boson is an essential component of the SM, which provide mass to the subatomic particles. However, we still have to learn a lot about the origin of the mass.
The strongest force in the universe is the strong nuclear force, a fundamental force which describes the interactions between quarks, gluons (both carry color charges) and nucleons inside the nucleus. Quantum Chromodynamics (QCD) is the theory of strong interactions which was formulated on an analogy to Quantum Electrodynamics (QED), the quantum theory to describe the electromagnetic force. QCD is a non-abelian gauge theory in which SU(3) group describes the three color charges of the strong force. In QCD, quarks interact with each other by an exchange of gluons. The interaction strength depends on the coupling constant α_s which is not a constant but it decreases with increasing momentum transfer (Q^2). At large momentum transfer, the coupling constant α_s becomes smaller and the quarks and gluons behave almost like a free particle. This phenomenon is known as asymptotic freedom. Hence, in this momentum transfer region, the perturbation theory can be applied. However, for small momentum transfer, the coupling constant becomes large and an infinite amount of energy is required to separate two quarks so the perturbation theory cannot be applied. The QCD coupling constant α_s as a fuction of momentum transfer is shown in the Figure 1.1 and is defined as follows:

$$\alpha_s = \frac{g_s^2}{4\pi} = \frac{1}{(33 - 2N_f)\ln(\frac{Q^2}{\Lambda^2_{QCD}})} \tag{1.1}$$

Where, g_s is the strong charge in the gauge group, N_f is the num-

ber of quarks and flavors and Λ^2_{QCD} is the renormalization constant, called as QCD scale [4]. The Λ^2_{QCD} divides the QCD physics into two regimes, low energy non-perturbative QCD (Effective field Theory) and high energy QCD where perturbation theories are applicable. In the low energy QCD, the degrees of freedom are hadrons. The study of the specific properties of hadrons like magnetic moments, form factor, polarizability, mixing angles of quark and gluon combinations in their wave functions etc can assist in understanding the problems in low energy QCD [5].

The physics program of the Wide Angle Shower Apparatus at Cooler SYnchrotron (WASA-at-COSY) investigates the symmetries and symmetry breaking patterns via the study of rare decays of light mesons π^0, η, η' and ω and the hadron structures [27]. Symmetry and its breaking can govern the character of the underlying interactions, therefore, it helps to better understand the strong interaction. This thesis aims to measure the transition form factor of the η meson, which is acessible through its rare decay $\eta \to e^+e^-\gamma$. The transition form factor gives an insight about the internal structure of hadrons.

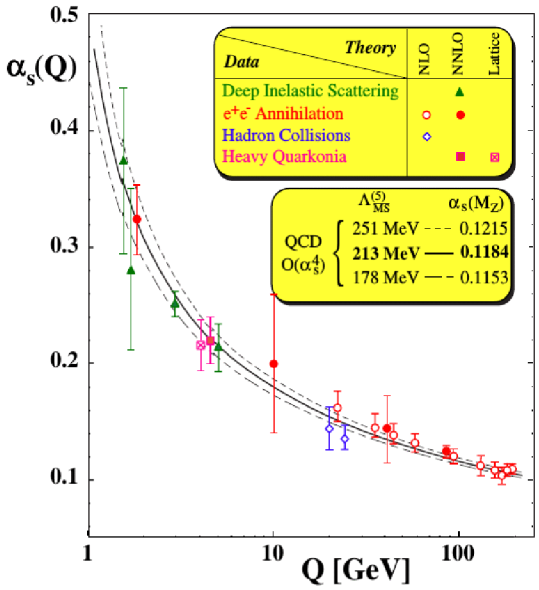

Figure 1.2. The QCD coupling constant as a function of momentum transfer. The figure shows both the experimental data and the theoretical predictions. Image is taken from reference [6]

1.2 η meson

The η meson is a pseudoscalar meson. It was discovered in the 1960s at the Berkeley Bevatron [7] in the $\pi^+ d \to pp\pi^+\pi^-\pi^0$ reaction. Its main characteristics are listed in the Table 1.1. The lightest three quarks (up, down, and strange) exhibit approximate SU(3) flavor symmetry [8], which gives rise to nine possible quark-antiquark bound states, grouped into an octet and a singlet state. These states form a light pseudoscalar meson nonet, shown in Figure 1.3. The η meson is a part of this pseudoscalar meson nonet.

Mass	547.862 ± 0.017 MeV
Quantum numbers $I^G(J^{PC})$	$0^+(0^{-+})$
Life time	$(5.0 \pm 0.3) \cdot 10^{-19}$ ns

Table 1.1. Main characteristics of the η meson.

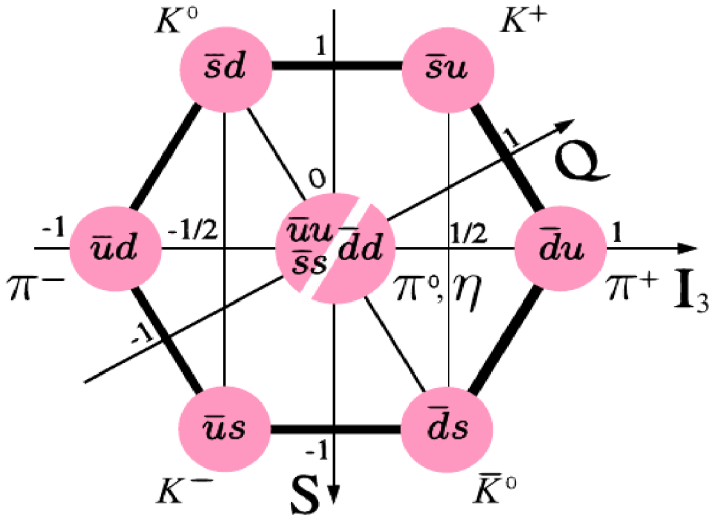

Figure 1.3. Pseudoscalar nonet

The η meson is a superposition of the octet ($\eta 8$) and singlet ($\eta 1$) states related by a mixing angle θ:

$$\eta = \eta 8 \cos(\theta) - \eta 1 \sin(\theta) \tag{1.2}$$

where,

$$\eta 8 = \frac{1}{\sqrt{6}}(u\bar{u} + d\bar{d} - 2s\bar{s}) \tag{1.3}$$

$$\eta 1 = \frac{1}{\sqrt{3}}(u\bar{u} + d\bar{d} + s\bar{s}) \tag{1.4}$$

Experimentally, the mixing angle has found to be $\theta \to 15.5 \pm 1.3$ [9]. The most prominent decay modes of the η meson are listed in the Table 1.2. The main decays are basically of two distinctive types, hadronic and radiative decays. All first order decays of the η meson are forbidden via strong, electromagnetic and weak interactions. The $\eta \to \gamma\gamma$ decay which is a second-order electromagnetic transition is the only allowed decay mode of the η meson.

Decay modes	Branching ratio
$\eta \to \gamma\gamma$	$39.30 \pm 0.20\%$
$\eta \to \pi^0\pi^0\pi^0$	$32.56 \pm 0.23\%$
$\eta \to \pi^+\pi^-\pi^0$	$22.73 \pm 0.28\%$
$\eta \to \pi^+\pi^-\gamma$	$4.60 \pm 0.16\%$
$\eta \to e^+e^-\gamma$	$(7.0 \pm 0.7) \cdot 10^{-3}$

Table 1.2. Dominant decay modes of the η meson. For the branching ratios, see reference [10]

The η meson is an eigenstate of Charge conjugation (C) and Charge conjugation parity (CP) operators. The rare decay modes become experimentally accessible due to forbidden first order decays. This makes the study of rare (small branching ratios) decays and symmetry breaking decays possible.

1.3 The decay $\eta \to e^+e^-\gamma$ (Dalitz decay)

It is a Dalitz decay. As shown in Figure 1.5, a meson decays into a real and a virtual photon. Then, virtual photon converts into a lepton-anti-lepton pair (l^+l^-). This virtual photon carries the momentum transfer square (q^2) equals to the invariant mass of the l^+l^- pair:

$$q^2 = M^2_{l^+l^-} = (E_{l+} - E_{l-})^2 - (p_{l+} - p_{l-})^2 \tag{1.5}$$

Where, E stands for the particle's energy and p for the corresponding momentum vector.

This decay is extra special as it enables the study of the electromagnetic transition form factor of the meson.

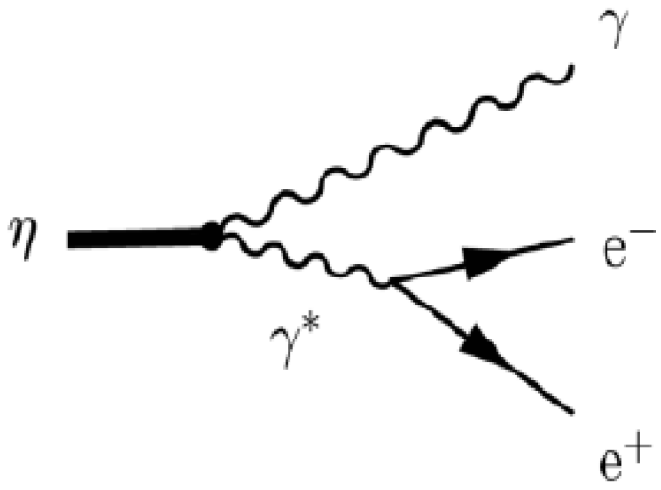

Figure 1.4. Feynman diagram of η Dalitz decay.

1.4 Electromagnetic transition form factor

The Rutherford scattering is a classical method to understand the structure of a particle. The form factor gives insight of the structure of a particle. In case of a charged particle, scattering is being done by means of a charged point-like probe on it. However, there are neutral (all charges are zero) particles present in the nature such as π^0, η, η', ρ^0, ω and ϕ. To study the structure of the neutral particles, scattering by charged particle does not serve the purpose. Therefore, for these particles their decays are studied. The differential cross-section for the scattering of an electron with a particle which has a structure, can be written as follows:

$$\frac{d\sigma}{dq^2} = |\frac{d\sigma}{dq^2}|_{QED} F(q^2)^2 \tag{1.6}$$

Where, $\frac{d\sigma}{dq^2}$ is the differential cross-section for the scattering of an electron with the composite particle and $F(q^2)^2$ is the form factor of the particle with a four-mometum transfer q^2, which also depends on it. The four-momentum transfer q^2 of the particle equates to the invariant mass of the dilepton pair ($M_{(l^+l^-)}$). $|\frac{d\sigma}{dq^2}|_{QED}$ is the differential cross-section for the scattering of an electron with the composite particle can be calculated within the Quantum Electro Dynamics (QED) framework. Hence, the form factor is the ratio of experimentally measured differential cross-section to the QED calculated differential cross-section. For a point like particle, the decay rate can be calculated within QED framework. However, the inner structure of the particle gives rise to the form factor. The dilepton mass spectrum within the QED framework was first derived by N.M. Kroll and W. Wada in the 1950s for the $\pi^0 \to e^+e^-\gamma$ decay [11], the corresponding expression [5] is given below:

$$\frac{d\Gamma}{dq^2.\Gamma_{\gamma\gamma}} = \frac{2\alpha}{3\pi q^2}\sqrt{\left(1-\frac{4M_l^2}{q^2}\right)\left(1+\frac{2M_l^2}{q^2}\right)\left(1-\frac{q^2}{M_P^2}\right)^3} F(q^2)^2 \tag{1.7}$$

Where, M_l is the mass of the lepton and M_P is the mass of the pseudoscalar meson.

When η decays into $e^+e^-\gamma$, the form factor describes the elctromagnetic structure arises at the transition vertex $\eta \to \gamma^*$. Hence, it is called the electromagnetic transition form factor. This decay holds a special place as this process involves only one pseudoscalar meson (η) at the transition vertex. Therefore, the form factor fully describe the structure of η meson.

1.4.1 Theoretical Models

There are various theoretical models to understand q^2 dependence of the transition form factor such as Vector-Meson Dominance Model (VDM), Constituent Quark Triangle Loop Model (QL), Dispersion theory which is a model independent approach, Brodsky-Lepage (BL) interpolation formula and Chiral Perturbation Theory (ChPT). Here, VMD and ChPT models are discussed in details.

Vector Meson Dominance (VMD) Model

The processes of electromagnetic interaction between photon and hadron takes place via the exchange of virtual photons. This vitual photon has same quantum numbers (spin, parity and charge conjugation) as neutral short-lived mesons, the lightest are the ρ^0 (m_{ρ^0} = 769 MeV), ω (m_ω = 783 MeV), and the ϕ meson (m_ϕ= 1020 MeV). Then, a virtual photon can interact with a hadron of interest via a transition to a virtual vector meson state, as shown in Figure 1.5. This concept was first found to occure in ep scattering and was confirmed by a number of other experiments too [5].

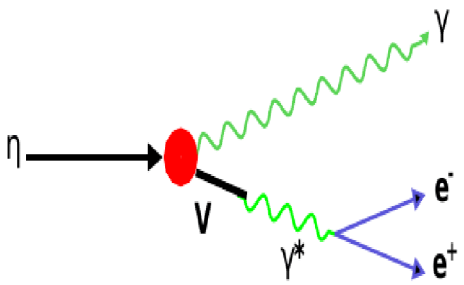

Figure 1.5. Feynman diagram of η Dalitz decay in VMD.

The form factor in the VMD according to Isobar model is as follows as in the equation 1.8. This model reports the resonances using Breit-Wigner formula [12].

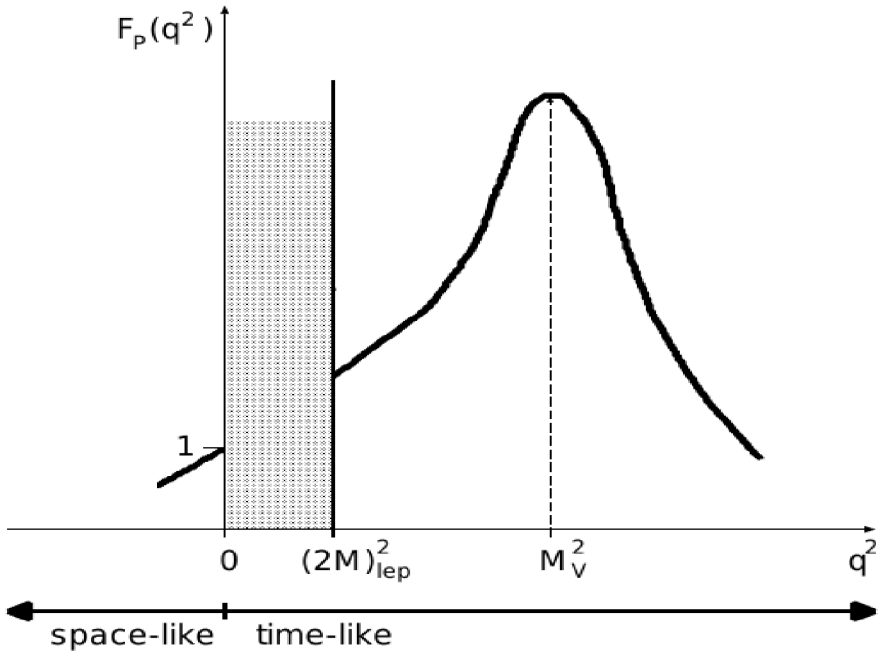

Figure 1.6. The qualitative behavior of electromagnetic transition form factor in the full kinematically accessible region of q^2. The shaded region is kinematically prohibited. The image is taken from [5].

$$F(q^2) = \sum_V \frac{M_V^2}{M_V^2 - q^2 - iM_V\Gamma_V(q^2)} \cong \frac{1}{1 - \frac{q^2}{M_V^2}} \tag{1.8}$$

where, $\Gamma_V(q^2)$ is the vector meson width and V stands for vector mesons (ω,ρ and ϕ). The Fourier transform of Eq.1.8 provide with the charge distribution inside of the meson. The study of the electromagnetic transition form factor in $A \to Bl_+l_-$ decays is strongly prominent in the time-like region, where the squared four-momentum of the virtual photon, q^2 is greater than $(2M_l)^2$. In this case the photon-hadron coupling is intensely pronounced.Here, the squared four-momentum, q^2 , approaches the squared mass of the vector meson ($q^2 \sim M_V^2$).The, the virtual meson reaches to its mass shell and becomes real. Further, it decays to a lepton pair. This results in a strong resonance enhancement of the form factor of a meson. Then, after passing the resonance, at $q^2 > M_V^2$, the form factor begins to diminish and whole process is illustrated in Figure 1.6.

The observed invariant mass distribution is fitted using a single-pole formula with a free parameter Λ which is related to the mass of the vector

meson [13]:

$$F(q^2) = (1 - \frac{q^2}{\Lambda^2})^{-1} = (1 - \frac{b^2}{q^2})^{-1} \tag{1.9}$$

In the limit of small q^2 , the form factor slope parameter, $b = \frac{1}{\Lambda^2}$ is associated with the radius of the pseudoscalar meson $b = \frac{<r^2>}{6}$. Here, r is the radius of the pseudoscalar meson [5].

Chiral Perturbation Theory (ChPT)

Chiral Perturbation theory is a QCD inspired model which allows to study the low-energy regime of QCD. The degrees of freedom in the low-energy regime of QCD are not quarks and gluons, but hadrons. The Lagrangian in ChPT is written in terms of the pseudo-Goldstone boson fields for pseudoscalar mesons. The form factor in ChPT is:

$$F(\Lambda_P, q^2) = \frac{\sqrt{2}C_P\alpha}{\pi f_\pi} \tag{1.10}$$

Where $C_\pi = 1$, $C_{\eta 8} = \frac{1}{\sqrt{3}}$ and $C_{\eta 1} = \frac{2\sqrt{2}}{3}$. The decay widths are expressed in terms of the parameters θ, f_1, f_8 and f_π.

$$F_\eta(q^2) = 1 + [\frac{2f_1 + f_8}{2f_1 + 2f_8} b_L + b_V]q^2 \tag{1.11}$$

$$b_L = -\frac{1}{24\pi^2 f^2}[1 + ln(m_k m_\pi)/\mu^2] = 0.32\ GeV^{-2} \tag{1.12}$$

Here μ^2 is mean vector meson mass and $b_V = 1/\mu^2 = 1.46 GeV^2$. The source of SU(3) breaking is f_1, f_8 and f_π. Using these equations the value out to be $\Lambda_\eta = 1.03\Lambda_\pi = 0.77$ GeV.

1.5 Previous Measurements

The transition form factor of the meson has been measured earlier by other experiments via $\eta \to \mu^+\mu^-\gamma$ and $\eta \to e^+e^-\gamma$ decays. The first measure-

ment of $\eta \to e^+e^-\gamma$ decay was done by optical spark chamber experiment at Rutherford Laboratory. They obtained the value of slope parameter $\Lambda^{-2} = -0.7 \pm 1.5$ GeV^{-2} based of 50 Dalitz decay events [14].

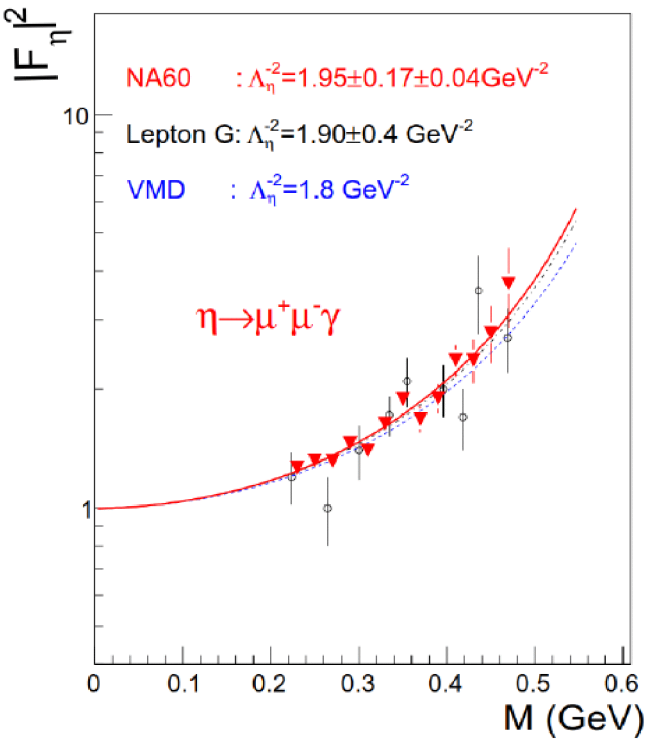

Figure 1.7. Measurements of the Lepton G (open circles) and the NA60 (triangles) experiment. The solid is fit to the NA60 data and the dotted lines are the VMD prediction [17].

Later on, NA60 experiment reconstructed approximately 9000 events of $\eta \to \mu^+\mu^-\gamma$ using the data taken in 2003 for In-In collisions and reported the value of $\Lambda^{-2} = (1.95 \pm 0.17_{stat} \pm 0.05_{syst})$ GeV^{-2} [15]. In this measurement, a large statistical uncertainty is observed in the higher M_{ll} region. They again reported an improved value of the slope parameter $\Lambda^{-2} = (1.951 \pm 0.059_{stat} \pm 0.042_{syst})$ GeV^{-2} (preliminary result) which is based on an analysis of 8×10^4 muon pairs produced in p-A collisions [16]. The same decay channel was also studied with the Lepton-G experiment, the result is shown in the Figure 1.7 [17].

Although, for the determination of the η meson transition form factor

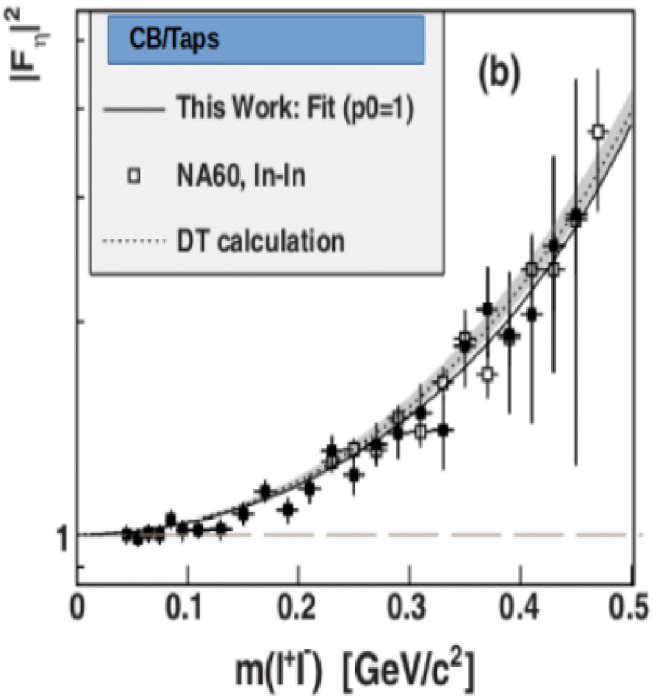

Figure 1.8. Measurements by the Crystal Ball (CB) and TAPS detectors (filled square) at MAMI-C accelerator (A2 collaboration) and NA60 (open square) experiment. The solid is fit to the CB-TAPS data and the dotted lines are from the Dispersion theory calculation.

using the $\eta \to \mu^+\mu^-\gamma$ Dalitz decay, a major shortcoming is to measure the form factor below the lower kinematic limit $q^2 = M_{ll} = 2M_\mu$. Whereas, $\eta \to e^+e^-\gamma$ Dalitz decay allows the measurement much closer to $M_{ll} = 0$ for the determination of the η transition form factor. In a measurement carried out via $\eta \to e^+e^-\gamma$ with the SND detector on the VEPP-2M collider in Novosibirsk [18], only 109 events were reconstructed. Another measurement was performed by the A2 collaboration at MAMI-C accelerator using the combined Crystal Ball (CB) and TAPS detectors, where, 1350 of $\eta \to e^+e^-\gamma$ events were reconstructed [19] and the value of $\Lambda^{-2} = (1.92 \pm 0.35_{stat} \pm 0.13_{syst})$ GeV^{-2} was reported. Later on, they reported $\Lambda^{-2} = (1.95 \pm 0.15_{stat} \pm 0.10_{syst})$ GeV^{-2} (preliminary result) in 2014 with an increased statistics of 2.2×10^4 $\eta \to e^+e^-\gamma$ reconstructed events [20], the result is shown in the Figure 1.8 [20]. However, they also report a need

for more precise measurement [20]. The most recent measurement is from CB-TAPS at MAMI-C experiment published in 2017. They report the value of the slope parameter $\Lambda^{-2} = (1.97 \pm 0.11_{tol})$ GeV^{-2} [21]. The recent measurement has smaller uncertainty than the previously measured values. The published data on the form factor of the η meson measurements, are listed in Table 1.4.

Experiment	Number of Events	Measured Reaction Channel	slope parameter Λ^{-2} $[GeV^{-2}]$
Rutherford Laboratory [14]	50	$\eta \to e^+e^-\gamma$	-0.7 ± 1.5
SND [18]	109	$\eta \to e^+e^-\gamma$	1.6 ± 2.0
LeptonG [17]	600	$\eta \to \mu^+\mu^-\gamma$	0.72 ± 0.09
NA-60 (2009) [15]	9000	$\eta \to \mu^+\mu^-\gamma$	$1.95 \pm 0.17_{stat} \pm 0.05_{syst}$
NA-60 New [16]	8×10^4	$\eta \to \mu^+\mu^-\gamma$	$1.95 \pm 0.059_{stat} \pm 0.042_{syst}$
CB-TAPS [19]	1350	$\eta \to e^+e^-\gamma$	$1.92 \pm 0.35_{stat} \pm 0.13_{syst}$
CB-TAPS [20]	2.2×10^4	$\eta \to e^+e^-\gamma$	$1.95 \pm 0.115_{stat} \pm 0.10_{syst}$
CB-TAPS [21]	5.4×10^4	$\eta \to e^+e^-\gamma$	$1.97 \pm 0.11_{tot}$

Table 1.3. List of slope parameter from various experiments

.

dataset	Number of Events	Measured Reaction Channel	slope parameter Λ^{-2} $[GeV^{-2}]$
pd→3Heη 2008	5.2×10^2	$\eta \to e^+e^-\gamma$	$2.27 \pm 0.73_{stat} \pm 0.46_{syst}$ [22]
pp→ppη 2008	3.1×10^3	$\eta \to e^+e^-\gamma$	$1.9 \pm 0.33_{stat}$ [23]
pp→ppη 2012	1.1×10^4	$\eta \to e^+e^-\gamma$	$1.97 \pm 0.29_{stat} \pm^{0.13_{syst}}_{0.23_{syst}}$ [24]

Table 1.4. List of slope parameter from previous WASA-at-COSY experiments. These are not published results.

The measurment has also been done by the WASA-at-COSY experiment previously. For the study, the η meson was produced in pp→ppη and pd→3Heη reactions in 2008, 2009 and 2012. The crosssection for pp→ppη is higher than the pd→3Heη. Which is a advantage in order to study rare decays. However, this has a disadvantage of large multi-pion background.

For pd→3Heη reaction the multi-pion production is less but also the statistics is small to study rare decays. The satistics was low in the study of pd→3Heη 2008, 525±26 events of the $\eta \to e^+e^-\gamma$ decay channel were reconstructed. The result from the study of pp→ppη 2008 dataset shows a background contribution in the lower momentum transfer region stemming from $\eta \to \gamma\gamma$ which could not be removed.

The data analysed in this work (pp→ppη 2010) is the largest dataset among all three datasets, therefore an improvement in the statistical uncertainty in the measurement is expected. The aim of this work is to calculate the transition form factor with improved statistical uncertainty. In addition, it will be checked if the result matches with the published results of other measurements.

Chapter 2

Experimental Setup

The Wide Angle Shower apparatus (WASA) is a fixed target experiment located at COSY (COoler SYnchrotron), Forschungszentrum Juelich, Germany. Figure 2.1 shows a Computer-Aided Design (CAD) of the WASA detector, the COSY beamline and the pellet target setup. The experiment has been designed to study both the production and the decay of the light mesons in hadronic interactions [25]. Experiment has a pellet target system with a target density of 10^{15}atoms/cm^2 which helps to achieve a luminosity equals to 10^{32} $cm^{-2}s^{-1}$. The high beam intensity and luminosity allow the study of rare decays of mesons. The CELSIUS/WASA experiment was initially built and operated at CELCIUS ring [26], Uppsala by an international collaboration of 60 collaborators from 15 different institutes. Later, it was brought to Germany in 2005. After the successful installation in 2006, it started taking data in April 2007. With increased energy and polarize beam, enhanced physics programme such as symmetry breaking [25] can also be studied with the WASA [27]. In this chapter we describe the WASA-at-COSY facility and the detector setup used in the experiment.

2.1 The COSY storage ring

The COSY [28] is a storage ring. It has a shape of a racetrack with two straight arms as shown in the Figure 2.2. It's circumference is 184 m. Including WASA, four internal experiments, beam cooling and, monitoring tools are placed on the straight sections of it. In addition, the beam can be delivered to external experiments as well. COSY provides both po-

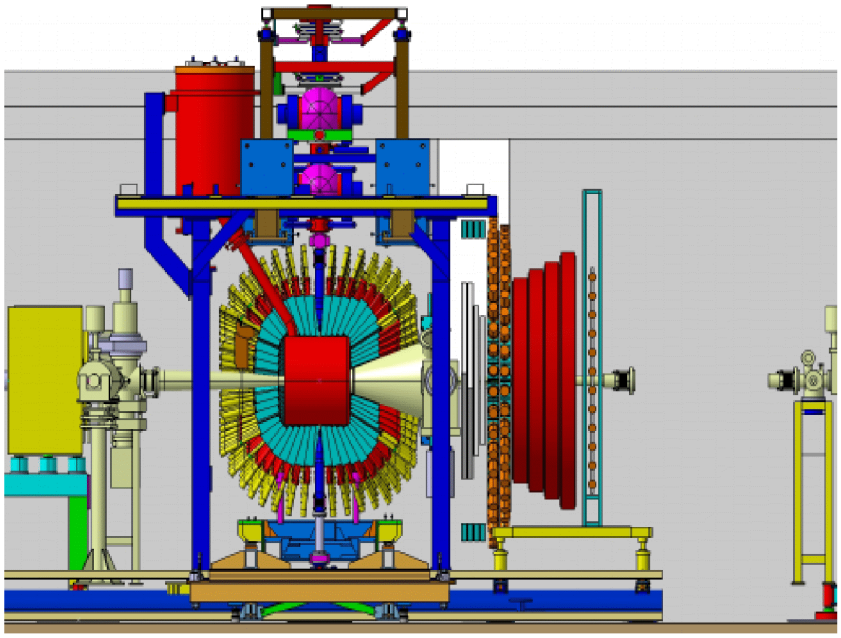

Figure 2.1. CAD drawing of WASA detector inside the COSY ring.

larised/unpolarised beam of proton and deutron in the momentum range 0.3 to 3.7 GeV/c [27]. Proton beam is produced by using H^- ions. The electrons are removed from Hydrogen atom by stripping in carbon foil of 20-25 $\mu m/cm^2$ thickness. Then, protons are preaccelerated up to 45 MeV [29] by a cyclotron and then injected into the COSY ring.

The beam cooling refers to a process where the momentum spread and emittance of the beam are reduced. the Internal pellet target results in the energy loss to the beam in each revolution. Due to a very effective beam cooling feature, a beam momentum resolution $\Delta P/P \sim 1.10^{-4}$ is achieved. The electron and stochastic cooling methods are insufficient to maintain the beam quality. Therefore, the accelerator runs in a barrier-bucket mode during data taking for WASA-at-COSY. In this mode, beam particles in the ring are grouped into a single bunch and the mean energy loss from interactions with the target is compensated with a radio-frequency cavity [30].

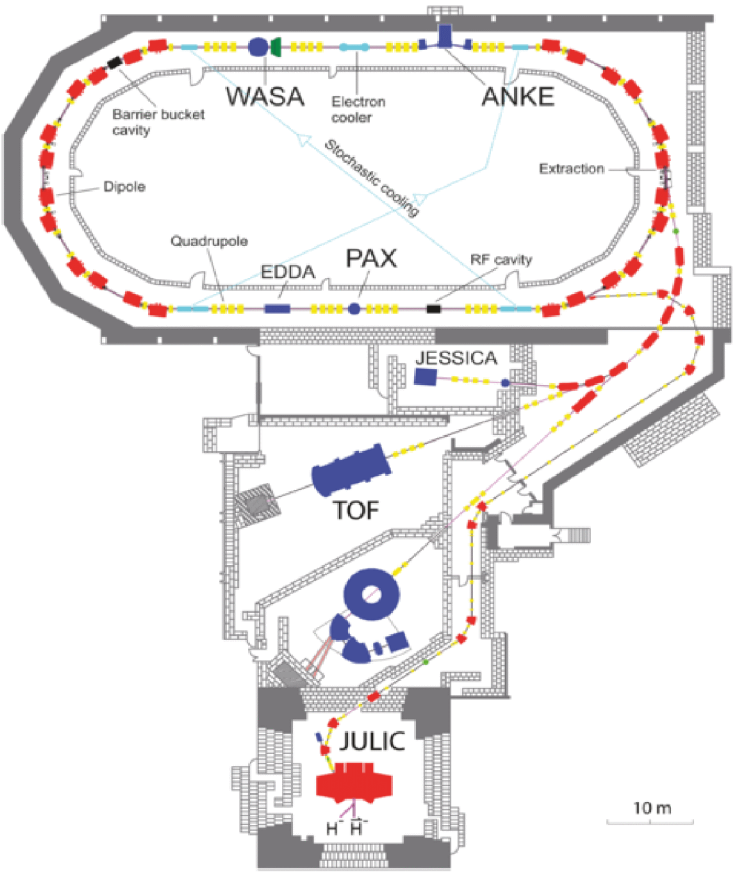

Figure 2.2. Floor plan of the COSY accelerator, showing the beam line and internal experiments like WASA, ANKE and PAX.

2.2 The Pellet Target

A high luminosity is required to study the rare decays of mesons. The pellet target at WASA provides the necessary requirement for this purpose. It has a thickness of $\sim 10^{15} atoms/cm^2$, which assist to achieve a luminosity of $10^{32} cm^{-2} s^{-1}$. The pellet target is illustrated in the Figure 2.3 . The top most part of the setup is the pellet generator. It converts liquified hydrogen and deuterium gas into droplets by vibrating glass nozzle. These droplets are frozen by evaporation in the droplet chamber and turned into solid spheres, called pellets. Pellets have a diameter of 35 μm, small size reduces the probability of secondary interactions. These pellets are collimated in a beam in the skimmer which is 2 m long and has a diameter of 7mm before entering the pellet tube. It has a mean velocity of 80 ms^{-1}. Pellet stream stops in the beam dump as shown in the Figure 2.4 after interaction with

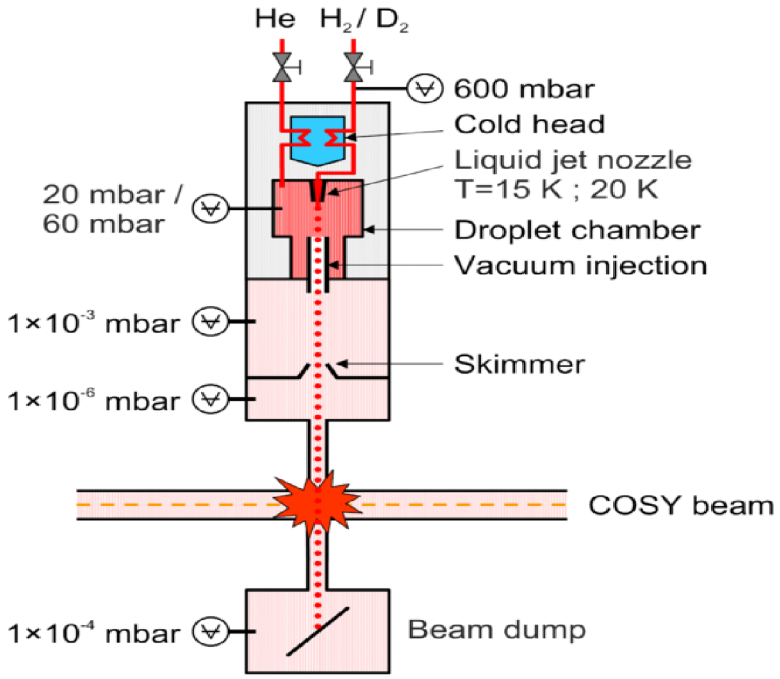

Figure 2.3. Schematic presentation of WASA-at-COSY pellet target [31].

the beam. A detailed description can be found in the reference [32].

2.3 The WASA Detector Setup

WASA is a fixed target experiment. It is designed to detect both neutral and charged particles. The detector setup is azimuthally symmetric. Recoil protons are reconstructed in the forward detector using the missing mass technique. The forward detector has a geometrical acceptance of 3° to 18°. The neutral and charged decay fragments of produced meson are reconstructed in the central detector. It's geometrical acceptance is 20° to 169°. Particles are measured in a right-handed polar coordinate system. The z-axis is parallel to the beam direction, the y-axis is parallel to the pellet stream, however, in the direction opposite to the pellet stream and x-axis remain perpendicular to both the axes and points out of the COSY ring. Schematic presentation of WASA detector setup is shown in the Figure 2.5. The detector components are described in detail in the following sections.

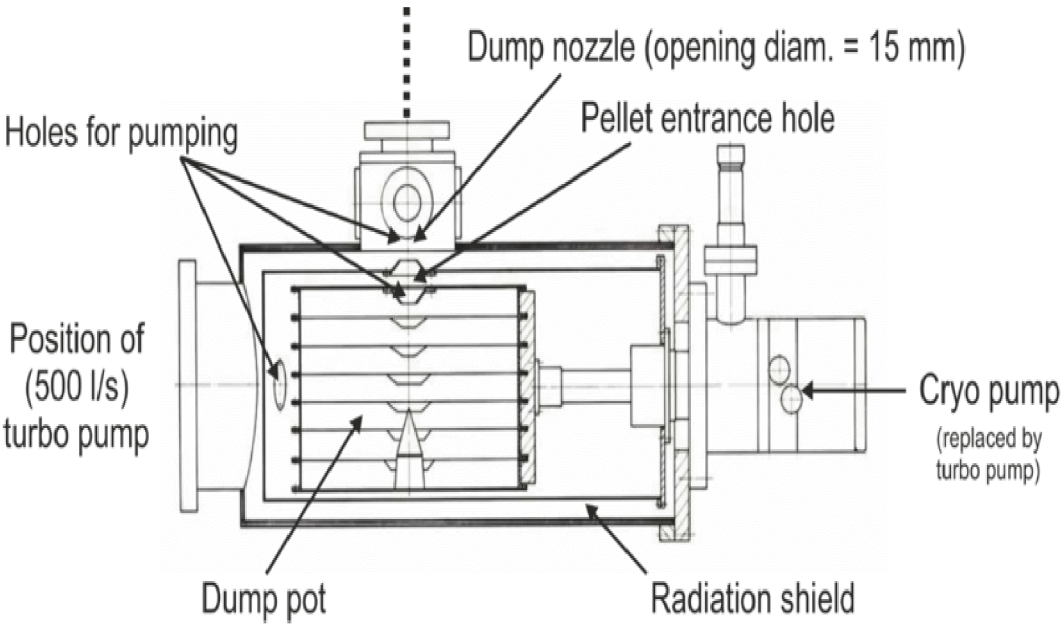

Figure 2.4. Schematic presentation of beam dump [31].

2.3.1 Forward Detectors (FD)

The forward detector is designed to detect the recoil particles such as proton, deuteron. It covers the polar angle from 3° to 18°. The components of FD are discussed in the following section.

Forward Window Chamber

The Forward Window Chamber is used in First level trigger. It is placed closest to the interaction region being the first layer of the forward detector. 48 plastic scintillators are arranged in two layers. Each layer consists of 24 elements and every element is shifted by half an element with respect to the other to provide better granularity. Scintillator elements are connected with PMT read outs. The first layer is placed with a small inclination with respect to the beam axis which fixes in the shape of the exit window of the central detector. A schematic view of FWC is shown in the Figure 2.6. A detailed description can be found in the reference [32].

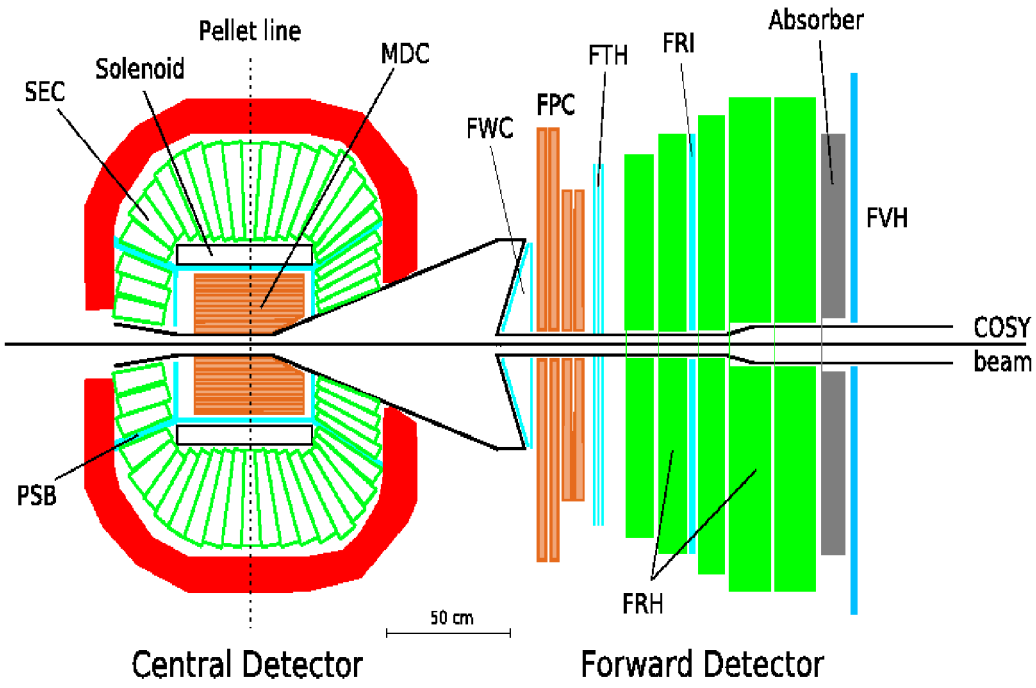

Figure 2.5. Schematic presentation of the WASA-at-COSY detector . Here, colors correspond to material types. Thin plastic scintillators are light blue, thick plastic scintillators are solid green, inorganic crystal scintillators are white with green outline, straw detectors are light brown. The iron return yoke is shown in red while other inactive components, such as the Superconducting Solenoid, Forward Range Absorber, and beam pipe are black or gray.

Forward Proportional Counter

The Forward Proportional Counter (FPC) is used for reconstructing the angles of the particle and placed after FWC. It's a tracking detector which has four modules. Each module has four layers, each layer has 122 straw tubes. These straw tubes have a diameter of 8mm and made up of 26 μm thick aluminized Mylar and a sensing wire of 20 μm stainless steel stretched with a tension of 40 g. The drift gas is a mixture of 80% Ar and 20% C_2H_6 . Each module is rotated by an angle of 45° with respect to other and perpendicular to the beam axis for achieveing better position resolution. The schematic view of one module of FPC is shown in the Figure 2.7. A detailed description can be found in the reference [32].

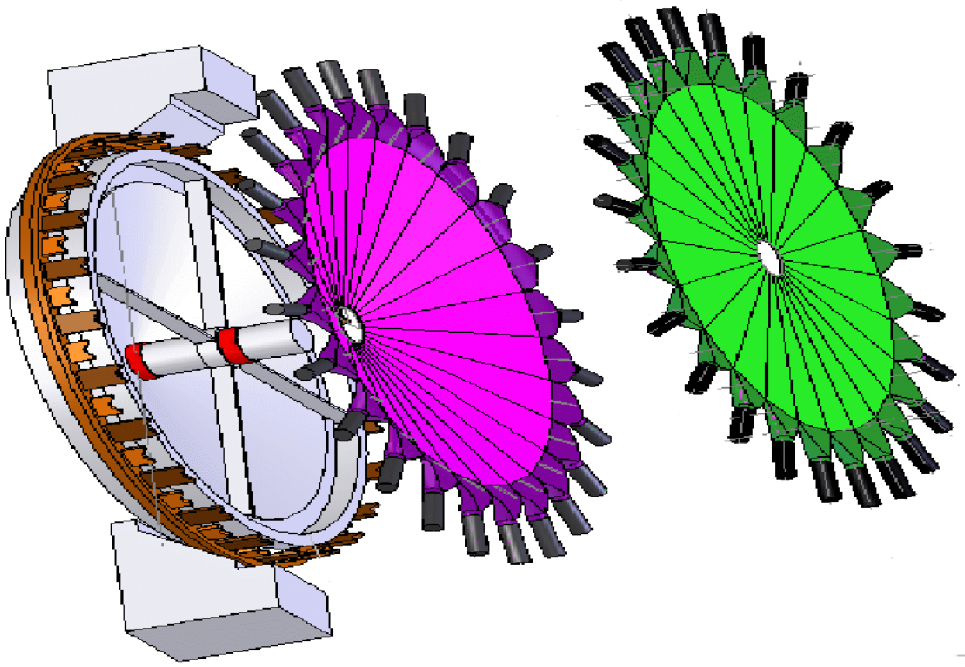

Figure 2.6. Schematic diagram of Forward Window Chamber.

Forward Trigger Hodoscope

A schematic view of Forward Trigger Hodoscope (FTH) is shown in the Figure 2.8. It is placed after FPC. FTH has three 5mm thick layers of BC 408 plastic scintillator. The first layer has 48 elements and the second and third layers have 24 Archemadian spiral shaped elements with a rotation in opposite directions. With each layer a readout PMT is connected. Together these layers provide a unique pixel structutre. FTH is used to calculate the hit multiplicity and to reconstruct θ and ϕ parameters of a track at the trigger level. A detailed description can be found in the reference [32].

Forward Range Hodoscope

The Forward Range Hodoscope (FRH) is placed after FTH. It is comprised of 5 thick BC400 plastic scintillator layers of diameter ranges from 1200 mm to 1800 mm. Each layer contains 24 elements, connected with read individually by XP2412 photomultiplier tubes for signal readout.

The thickness of first two layers is 11 cm and of last two layers is

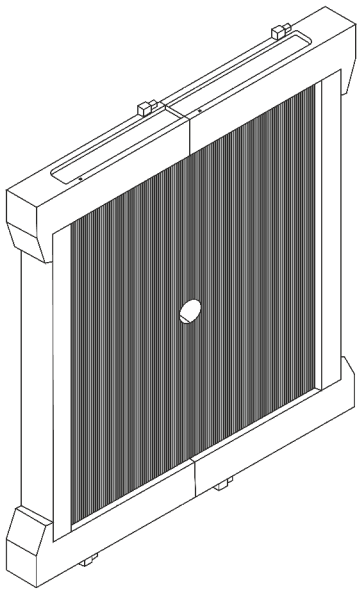

Figure 2.7. Schematic diagram of one module of Forward Proportional counter.

15cm. When particle passes through FRH, it deposits its energy in the layers of FRH. This information is used to identify charged particles using $\Delta E - \Delta E$ method and to calculate their initial kinetic energy. Different particles have different stopping power as listed in the Table 2.3.1. FRH also delivers fast signal for the first level trigger. A detailed description can be found in the reference [32].

Particle	Stopping power
π	200 MeV
p	360 MeV
d	450 MeV
^{3}He	1000 MeV
^{4}He	1100 MeV

Table 2.1. Stopping power of different type of particles.

Forward Range Intermediate Hodoscope

The Forward Range Intermediate Hodoscope (FRI) is placed between second and third layer of FRH. It consists of two layers and each layer has 32 plastic scintillator bars of 5 mm thickness. In the first layer, bars are arranged horizontally and in the second layer bars are arranged vertically

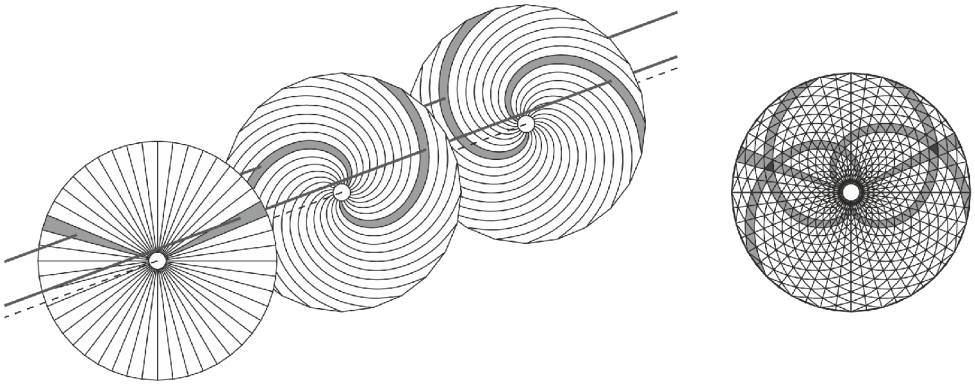

Figure 2.8. Schematic view of Forward Trigger Hodoscope. **Left Figure** shows three layers of FTH and two particles are hiting this detector component. **Right Figure** shows the overlaping of these three layers.

. This configuration compliments the position determination by FRH. A detailed description can be found in the reference [32].

Forward Range Absorber

The Forward range absorber (FRA) can be placed between FRH and Froward veto hodoscope (FVH). It has scintillators of variable thickness ranges from 5 mm to 100 mm, which can be adjusted during the experiment. In the $pp\eta$ production, slow protons are stopped in the FRA, however the fast protons from other reactions punch through it and produce a veto in FVH. A detailed description can be found in the reference [32].

Forward Veto Hodoscope

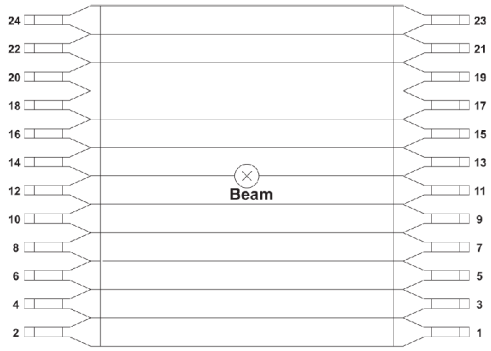

Figure 2.10. Schematic view of FVH.

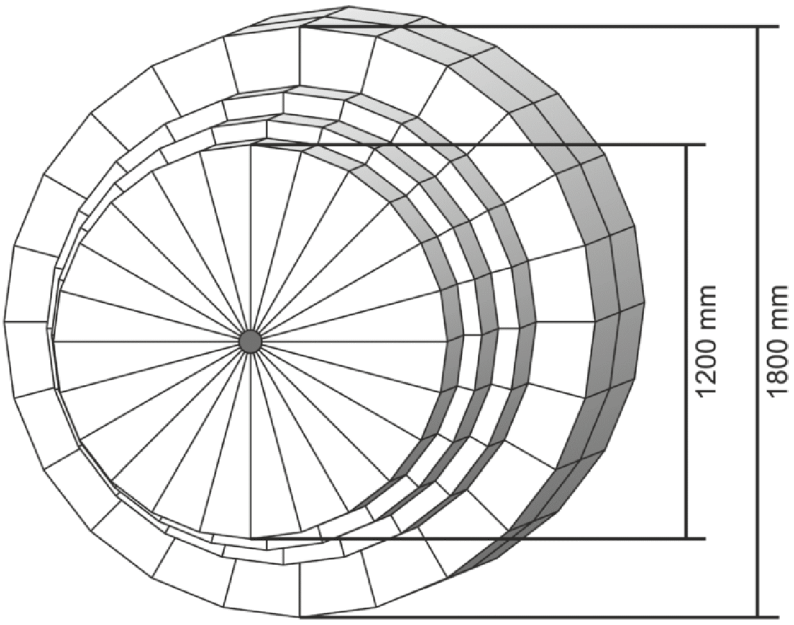

Figure 2.9. Schematic presentation of the Forward Range Hodoscope.

A schematic diagram of Forward veto hodoscope is shown in the Figure 2.10. FVH is the last element of the forward detector. It is made up of twelve horizontally arranged plastic scintillator barrels of 165 cm 13.7 cm 2 cm dimension. The signals from the FVH can be used as a veto for the selectivity of the trigger. A detailed description can be found in the reference [32].

2.3.2 Central Detectors (CD)

The central detector surrounds the beam-target interaction point. The detector is azimuthally symmetric and it covers a polar angle range of 20° - 169°. It is designed to detect and reconstruct the decay products ($e^{\pm}$, $\pi^{\pm}$, γ) of the produced mesons. The components of the CD are discussed in the following section.

Mini Drift Chamber (MDC)

The MDC is a tracking detector, surrounding the beampipe in the magnetic field of Solenoid. The acceptance of MDC in the polar angle is from 24° to

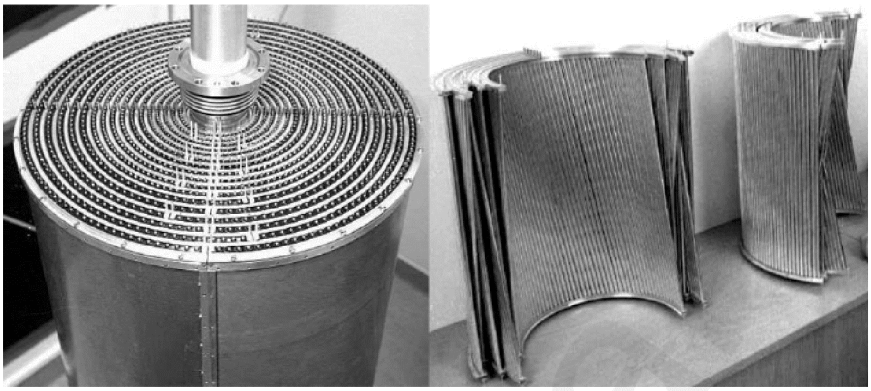

Figure 2.11. Schematic presentation of the MDC. Left: Assembled around the scattering chamber and enclosed by a Al-Be cylinder. Right: Drift tubes of the different MDC half layers.

159°. In MDC, 1738 drift tubes are arranged in 17 layers in a cylindrical shape. The straws in odd layers are parallel to the z-axis and in even layers make a small skew angles $(6° - 9°)$ with the z-axis. This assist for a measurement in three dimension. Each drift tube is made up of 25 μm thin aluminium mylar and 24 μm diameter wire of gold plated tugsten. The drift tubes are filled with the 80% ethane and 20% argon. The diameter of drift tudes is in a ascending order from inner most layer to outer most layer. The diameter of inner most and outermost layers ranges from 4 mm to 8 mm. The Solenoid provides an axial magnetic field that results the curved trajectory of the charged particles while passing through MDC. This enables to calculate the momentum of the charged particles. A schematic view of MDC is shown in the Figure 2.11. A detailed description can be found in the reference [32].

Plastic Scintillator Barrel (PSB)

The Plastic Scintillator Barrel is made up from 8 mm thick BC408 plastic scintillator. It is situated around the MDC and consists of three parts: central, Forward and backward endcap. The forward and backward parts conprises 48 trapezoidal shaped elements and central part has 52 bars. The central part is parallel to beam direction, forming two layers with a

small overlap between elements. The forward end cap is perpendicular to the beam axis while the backward end cap is inclined at an angle of 30 degree with the beam axis, to form a conical surface. Both the forward and backward endcaps has holes of 19 cm and 12 cm diameter to accomodate the beampipe. Each scintillator is connected to a light guide coupled to the photo-multiplier tube. PMTs are kept outside of the iron yoke in order to shield them from the magnetic field. The PSB provides fast signals for the first level trigger. Along with the MDC and the Calorimeter, it assist for the charge particle identification. A schematic view of FWC is shown in the Figure 2.12. A detailed description can be found in the reference [32].

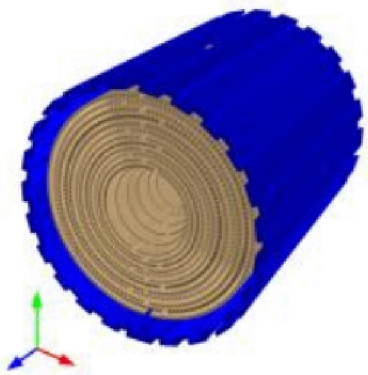

Figure 2.12. 3D diagram of the central part of PSB, encircling the MDC.

Superconducting Solenoid

The Superconducting Solenoid encloses the volume of the MDC and the PSB and produces maximum 1.3 T axial magnetic field in the direction of beam axis. It operates in a persistent current mode with a small helium refrigerator. The return path for the magnetic flux is provided by a yoke made out of 5 tons of soft iron with a low carbon content. The yoke also enables the shielding of the readout electronics from the magnetic field and serves as a mechanical support for the calorimeter crystals. Along with the MDC, it helps to measure the momentum of the charged particles. A detailed description can be found in the reference [32].

Scintillating Electromagnetic Calorimeter (SEC)

The Scintillating Electromagnetic Calorimeter is the outer most component of the central detector. The total polar angular coverage of SEC is from 20° to 169° and total azimuthal coverage is 4π which provide 96% geometrical acceptance. In the calorimeter, 1021 sodium doped CsI trappezoidal shaped crystals are assembled in 24 rings. These crystals have 16 radiation lengths and 0.8 hadronic interaction lengths. Each crystal covers 5% polar angle and 7.5% azimuthal angle. The detector consists of mainly three parts, forward, central and backward including necessary gaps for pellet beam pipe and helium supply for the solenoid. The forward part is comprised of four rings with 36 crystal elements each, the central part consists of 17 rings with 48 crystal elements each and and the backward part has three rings of which two have 24 crystal elements and the one has twelve elements. The photomultiplier tube is connected to each crystal element by long light guides in order to keep the readout outside the iron yoke. SEC can reconstruct both photons and charged particles upto 800 MeV. The relative energy resolution of the photon is $\sigma(E)/E = 5\%/\sqrt{E}$ and for stopped charged particle is $\sim 3\%$. A schematic view of FWC is shown in the Figure 3.4. A detailed description can be found in the reference [32].

2.4 Data Aquisition System (DAQ)

The WASA data aquisition system is based on the third generation of the DAQ systems for the experiments operated at COSY. It is designed to handle the luminocities achieved in the experiment. The DAQ is responsible for the signal readouts from each detector components, their digitization and then provide in a suitable format for further analysis. A schematic presentation of DAQ is shown in the Figure 2.14. Depending upon the detector component, the signal shape and time properties varies, for e.g. the calorimeter crystals provide slow signal, whereas the signal from the plastic scintillators in PSB and forward detector is faster. Signals from

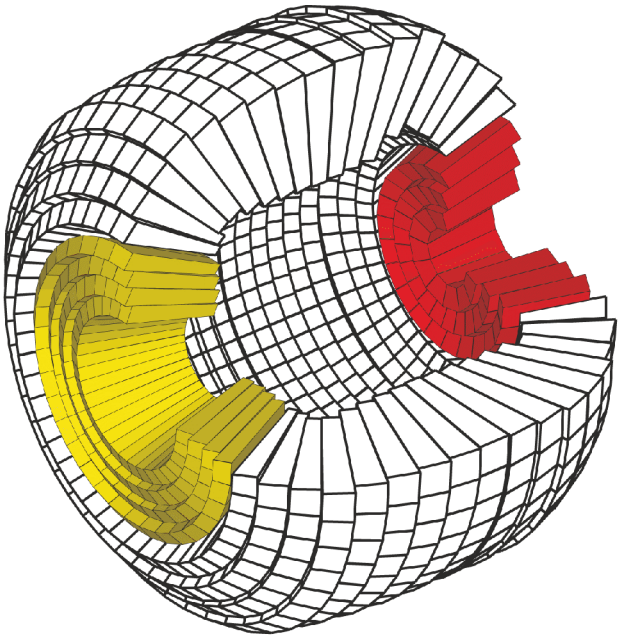

Figure 2.13. Cross-sectional view of SEC. The white, red and blue colour represents the central, left and right part respectively.

PMTs of calorimeter is divided in two parts using a splitter. This signal goes to S-QDC (Slow Charge to Digital converter) module with a sampling rate of 80 MHz and then finally goes to trigger board after passing through the discriminator. Fast QCD is used for the plastic scintillator detector, which has a sampling rate of 160 MHz. According to the timing properties, two different types of TDC modules(Time to Digital convertor) are used. Slow TDC modules based on GPX-TDC chip are used for straw chambers and fast TDC modules based on F1 ASIC are used for plastic scintillator detectors. All digitizing modules work in self triggering mode. After the digitization, trigger system issues a trigger. Then, synchronization system generates an event number with a time stamp and send to the digitizing modules. A detailed description can be found in the reference [32].

2.5 Trigger System

WASA experiment runs with a high luminocity which results a event rate of ∼5 MHz. The data aquisition system allows the readout upto ∼ 20 kHz.

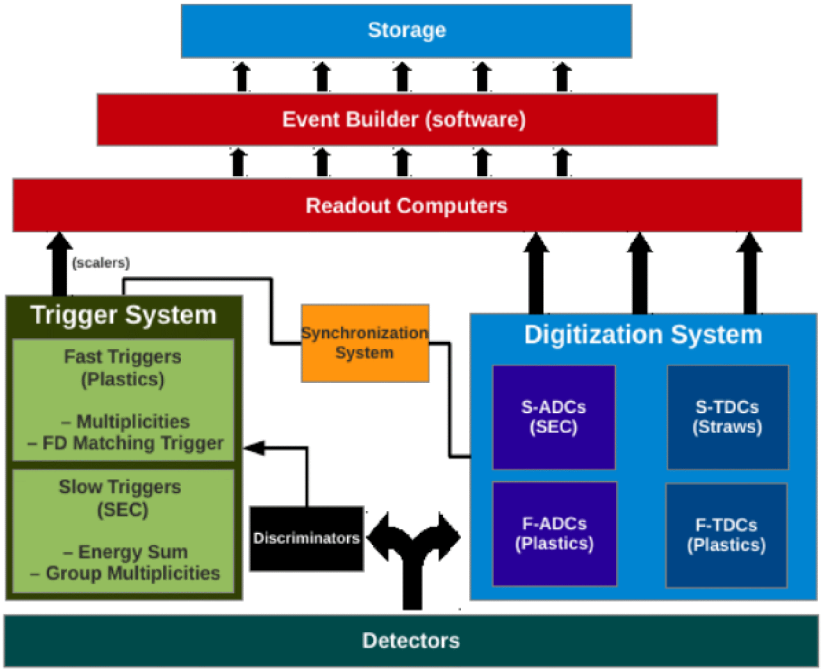

Figure 2.14. Schematic presentation of data aquisition system used by WASA-at-COSY.

Therefore a trigger system is required to select maximum events of interest. A three level trigger system is used here. The trigger selection is based on the multiplicities, time coincidences, and track alignments in the plastic scintillator detectors on the first level trigger as well as cluster multiplicities and energy sums in the calorimeter for the second level trigger. These are hardware triggers and can also be prescaled in order to reduce the number of events.

In addtion, a third level software based trigger is implemented for the event reconstruction. The software triggers are basic selection conditions on the different detector elements, combined by an AND-logic.

Following trigger conditions are implemented for the event selection of pp$\rightarrow$ $ppe^+e^-\gamma$ reaction:

1. At least two hits in the second FRH element are above a given energy threshold corresponds to two protons in the Forward Detector.

2. At least two clusters in the Plastic Scintillator Barrel above a given energy threshold corresponds to charged tracks in the Central Detec-

tor.

3. At least one cluster in the calorimeter is above a given energy threshold corrsponds to photon.

2.6 Analysis tools

Main tools for the simulation are Pluto++ and WASA Monte Carlo, However, RootSorter is used for the analysis of both the simulated and experimental data. The softwares used for analysis are illustruted in the following sections and the data processing flow during the anlysis is shown in the Figure 2.15.

2.6.1 Pluto++

Pluto++ is a Monte Carlo simulation tool for heavy ion and hadronic-physics reactions [33]. The reaction can be generated from pion production threshold to intermediate energies of a few GeV per nucleon. The software is based on Root analysis framework and was intially developed by High Acceptance Di-Electron Spectrometer (HADES) collaboration [34]. It provides a set of C++ classes such such as particles, reactions and interfaces for event generation. The input for Pluto are the beam projectile, target, fainal state particles and the beam kinetic energy. The reaction is generated on an event by event basis according to a homogeneous and isotropic phase space using the Genbod algorithm which calculates the phase space of N-body decay [35]. The events are generated by resonance production with mass-dependent Breit-Wigner sampling. The output file is produced in a root format, however the file format can be adjusted. The package is quite flexible as it also allows the inclusion of new model.

2.6.2 WASA Monte Carlo (WMC)

The output of Pluto++ serves as a input for WMC. However, the WMC can also simulate a type of particles with energy and direction in a specific range. The software is based on GEometry ANd Tracking (GEANT) package which was originally developed in CERN [36] for high energy experiments. The GEANT3 software contains the description of vaious physical processes of interaction of particle with the detector medium. It also contains the definition of multiple scatterings within the medium and the conversion in the detector material. All WASA detector components are implemented within GEANT3. The output from the WMC are saved in a format similar to the experimental data. In addition, the output data has the information of original final state momenta and track banks with the true information of the event which enables in finding out the reconstruction efficiency, detector acceptance and the resolution.

2.6.3 RootSorter

The RootSorter is an analysis pakage, which was developed by COSY-Apparatus for Studies of Nucleon and Kaon Ejectiles (ANKE) collaboration [37]. It is based on ROOT data analysis framework. Root [38] is a object-oriented C++ software, was initially developed by European centre of nuclear physics research (CERN) in order to analyse the high energy particle physics data. The functions of root consists of tools for data handling, event processing and histogram fitting etc. Both online and offline data analysis for WASA is done within RootSorter. The C++ classes in the RootSorter are responsible for the data storage and particle track reconstruction. Figure 2.15 shows the data processing procedure in the RootSorter. The hits in each detector components are stored in a object class, known as Hit Banks. The experimental data is stored in the hit banks known as RawHitBank to be calibrated and the Monte Carlo data is stored into in the hit banks known as a MCHitBank. A steering is done on Monte Carlo data by means of filters to match its resolution to the experimental

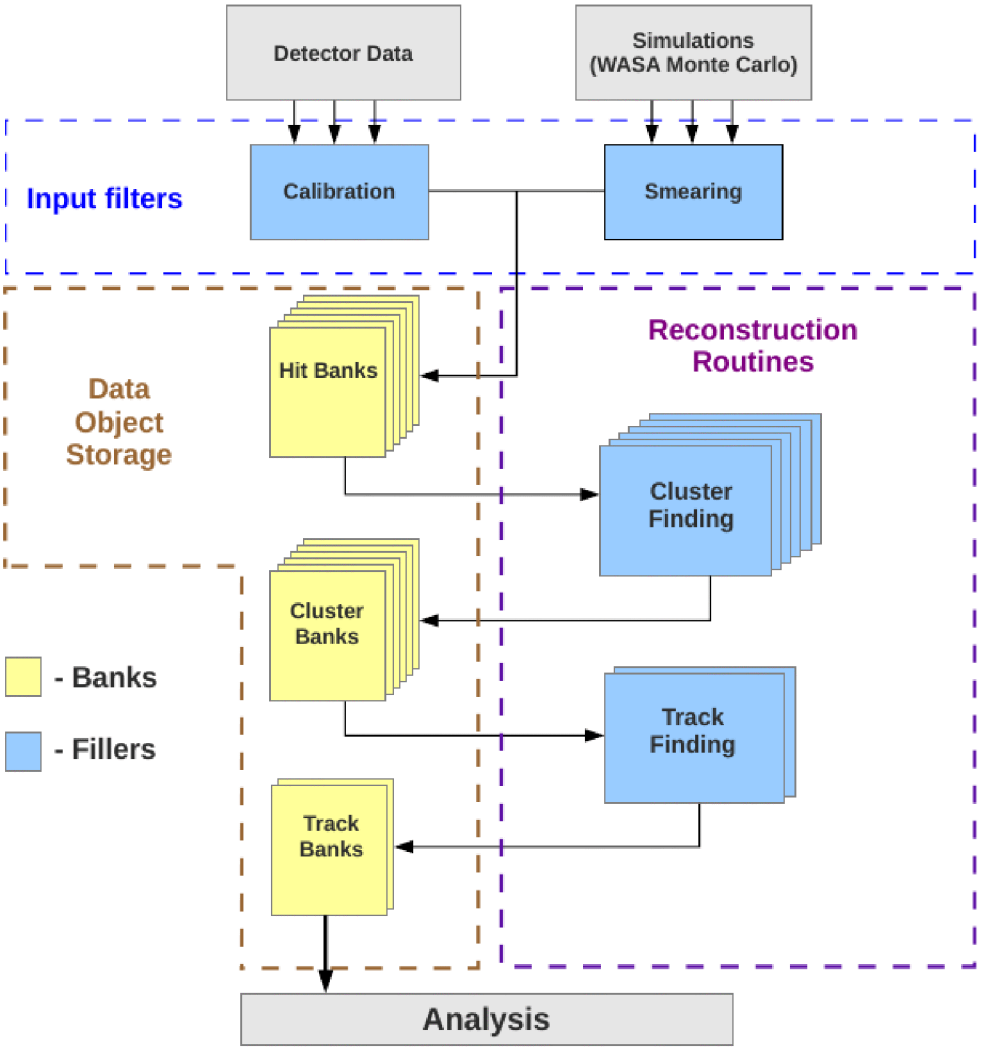

Figure 2.15. Schematic presentation of flow of data during analysis.

resolution by applying smearing factors. After calibration or filtering, data from experiment and simulation are handeled identically. Further, the hits are grouped into clusters by cluster finding routine and are stored in cluster banks. These cluster are used to reconstruct the tracks of particles by track finding routines. Finally, tracks are stored in the track bank and are called in data analysis.

Chapter 3

Event reconstruction

The digitized information from each sub-detector is stored on the hard disk for high level analysis. As the data from each detector element is stored in ADC (analog-to-digital converter) and time information in TDC (time-to-digital-converter) form, these informations need to be translated in corresponding energy (GeV) and time values (ns). The conversion from digitized signal to the units of energy or time is not accurate, therefore, the data needs to be calibrated. After the conversion, the informations are combined to reconstruct the track and energy of those particles. This is called event reconstruction. The kinematic information is used to perform physics analysis after event reconstruction. The methods of calibration and the reconstruction of the energy-momentum four-vector of different particles going in the forward and central detector are discussed in this chapter.

3.1 Forward Detector

The recoil protons are identified in the forward detector. The FD consists of FWC, FRH and FPC, which are used for the track and energy reconstruction procedure. These detector parts has to be calibrated. The calibration and track recnstruction method of FD is discussed here.

3.1.1 Calibration

In the calibration method, the conversion factors are generated for individual detector elements which relates the ADC and TDC values into GeV and ns and then parametrised by calibration constants. When a charged particle passes through matter, it interacts with the valance electrons of the atoms of the interacting matter and ionize them. In this process, the particle losses some of its energy which depends on the mass, electronic charge and energy of the particle. Different particles leave distinct patterns of energy loss in layers of the detector within the non-relativistic regime when passes through it, This phenomenon assist for the identification of the particles and calibration. The energy loss by the particle can be calculated using the Bethe-Bloch formula as given in the Equation 3.1 [41].

$$-\frac{1}{\rho}\left\langle\frac{dE}{dx}\right\rangle = k\frac{Z}{A}\frac{z^2}{\beta^2}\left[\frac{1}{2}ln\left(\frac{2m_e c^2\beta^2\gamma^2 T_{max}}{I^2}\right) - \beta^2 - \frac{\delta(\beta\gamma)}{2}\right] \tag{3.1}$$

$$\beta^2 = \frac{v^2}{c^2},\ \gamma^2 = \frac{1}{1-\beta^2} \tag{3.2}$$

In equation 3.1, k is a constant. Z, A and ρ represent the atomic number, atomic mass and density of the interacting matter. I is the mean excitation energy. z, m and v stands for the charge, rest mass and the velocity of the particle. T_{max} is the maximum kinetic energy transferred from the charge particle to an electron of the atom of the interacting matter, e and m_e are the charge and mass of electron. With the help of Eq. 3.1 initial kinetic energy of the particle also can be estimated.

The calibration of forward detector is optimized with protons. It is done in two parts. (1)Non-uniformity correction and (2)Non-linearity correction.

The FD mainly consists of layers of plastic scintillator. When the particle interact with the scintillators, emits light. The energy loss of the particle is calculated by the emitted light output. However, there is a possibility of light getting absorbed inside the scintillator crystal which causes a loss in the light output to be collected at the periphery. All the photomultiplier tubes (PMTs) are situated at the boundary of the crystals, so the light out-

put is smaller at small scattering angles than at the large scattering angles. This results a non-uniform light collection. Fast protons produced in pp elastic scattering are used for non-uniformity corrections. As being a minimum ionizing particles, their energy loss is constant per unit length. The light output of each element of all the layers is parametrized as a function of the scattering angle for obtaning the non-uniformity correction factors. Quenching effects and PMT's non-linear responses causes a non-linearity. For non-linearity corrections, the deposited energy in one layer of the forward detector is plotted with respect to next layer. This procedure is done for all layers. Then the proton band in the corresponding ΔE-ΔE plot is compared with the position of the proton band in the simulation and the correction factors are calculated and used for the calibration. For a more detailed calibration procedure of the FD, see the reference [39].

3.1.2 Track Reconstruction

Track reconstruction is a procedure to determine the trajectory of a particle inside the detector using the hit information from detector elements. The individual hits in each plane of the forward detector are combined to form the cluster. To form a cluster, the time coincidences of individual hit with the hits in the adjacent element of the plane is taken into account. The energy of the cluster is a sum of the energies of hits. The time and angle values are the average of the coresponding values of the hits of the corresponding cluster respectively. The track of a particle is reconstruceted using these clusters. FPC and FTH are used for reconstructing the angles of the particle as they provide a good angular resolution. If there is a geometrical overlap between the FTH and the FPC then the angular information (both the polar and the azimuthal) of a particle track is improved by a factor of two [42]. When the particle passes through layers of the forward detector, it deposits a fraction of its energy in each layer. The energy of the track is the sum of deposited energies in all FTH and FRH layers.

3.2 Central Detector

3.2.1 Mini Drift Chamber

Calibration

The track of the charged particle, which enters at some angle (other than 0 deg or 90deg with respect to the magnetic field direction) in a magnetic field, follows a helical path. The direction and trajectory of the path can be determined by the Lorentz force equation. In the MDC such helix is defined by five parameters namely r, z_0 ,d_0, ϕ_0 and cotθ. Among these parameters r, z_0 and d_0 provide the axial information and can be describe as follows: If the helix is projected to the x-y plane then the radius of the circle is defined as r as shown in Figure 3.1. The distance between the closest point

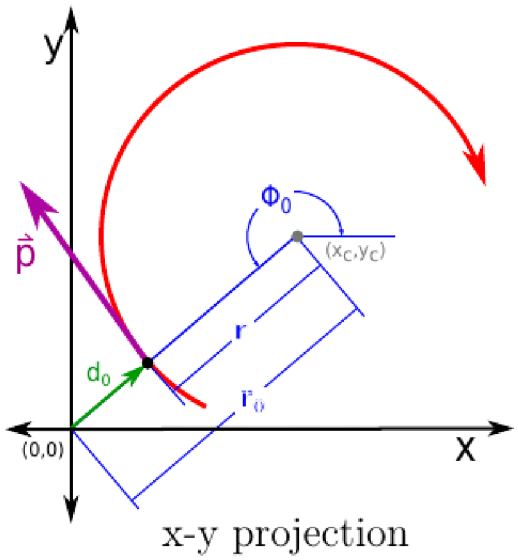

Figure 3.1. Projection of the helix to the x-y plane.

of the helical path and the origin is the parameter d_0 whereas the angle ϕ_0 is the relative orientation of the center of helix and origin as shown in the Figure 3.1. The z coordinate of the pivot point is defined as z_0 and the cotθ defined the polar angle of the particle. These two parameters are described clearly in the x-z and s-z Figure 3.2. Here, s is the path length of the helix and defined as $s = 2\pi r$. The track momentum is calculated at the pivot

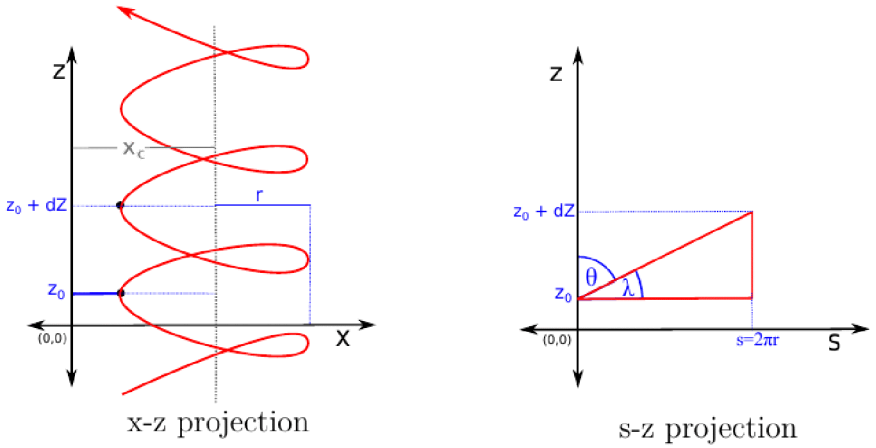

Figure 3.2. Projection of the helix to the x-z and s-z plane.

point. In order to determine the magnitude of the momentum vector the Lorentz force equation is used. Neglecting the effect of the electric field on the charged particle and considering B is parallel to z axis, the Lorentz force equation can be written as $F = qvB$. By equating the centripetal force to the Lorentz force :

$$Mv^2/r = qvB \tag{3.3}$$

Which gives total momentum: $p_t = (2.98 \times 10^{-2})rB$. The Track momentum vector can be deduced from the above mentioned helix parameters as follows:

$$p_x = p_t \cos\phi_0$$
$$p_y = p_t \sin\phi_0$$
$$p_z = p_t \cot\theta$$

The MDC consists of drift tubes (also called as straws) and the sensing wire. The wire is situated at the center of these straws. A signal from the cascade produced by particles which are close to the wire will be immediately detected as compared to those passing through the edge of the straw. Depending upon the diameter of the straw, the time for the cascade to reach the sensing wire can be between 100-200 ns and is known as drift time. The position information can be further improved by taking into account this drift time. The closest approach of the particle to the wire

is called the drift distance. The drift distance is calculated using the drift time information. Time calibration is performed in two steps. The time distribution of hits in each straw with respect to the PSB time is measured in the first step. In the second step, a time window is defined around the distribution for possible drift time range. Then, the time window is mapped with respect to the possible drift distance. For each straw, the parameters of the mapping function are stored in a file and used to calibrate hits.

3.2.2 Plastic Scintillator Barrel

The energy loss by a charged particle in a plastic scintillator is described by Equation 3.1. This deposited energy is corrected for the particle's path length. The energy deposits is transformed from charge-to-digital converter (QDC) units to MeV. The path length is a function of the polar angle of the particle. For the PSB calibration, pions are used as those are produced in majority. The energy loss per unit path length with respect to the MDC mometum is plotted in the left hand side Figure 3.3. The pion is a minimum ionizing particle above the momentum of 250 MeV/c, hence, it lose a constant energy after reaching this limit. The calibration constants are calculated for each element. To determine the calibration, the peak position in simulation is matched the data. In order to determine the calibration parameters are determined by parameterizing energy deposit per unit path length as a function of polar angle.

3.2.3 Scintillator Electromagnetic Calorimeter

The SEC is designed to measure the energy of the electrons and the photons. The calibration is performed using the neutral pion decay $\pi^0 \rightarrow \gamma\gamma$. The pions, produced in proton proton reaction at a kinetic beam energy of 500 MeV, are used for this purpose. Events with exactly two photons in SEC are selected for the measurment. Pions are tagged using these two photons. The invariant mass is calculated for each pair of photon using the

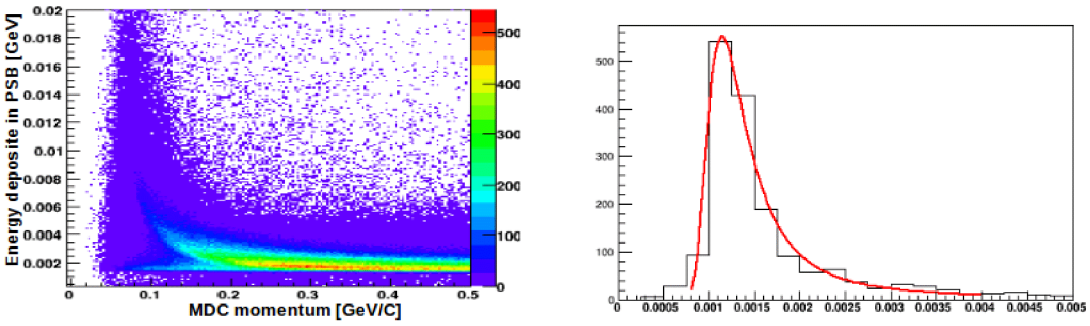

Figure 3.3. Left: Energy loss per unit path length with respect to the MDC mometum, Right: Projection for one element of PSB. Red curve is fitting function (Landau function).

following Equation:

$$M_{\gamma 1 \gamma 2} = \sqrt{2kE_{\gamma 1}E_{\gamma 2}(1 - cos\theta_{1,2})} \tag{3.4}$$

Where, $E_{\gamma 1}$ and $E_{\gamma 2}$ are the measured energies of the photons, $\theta_{1,2}$ is the opening angle and k is a global correction factor. The correction factors are derived based on the idea that the invariant mass of two photons should be at the π^0 mass (π^0 mass is 0.135 GeV/c^2). Figure 3.4 shows the invariant mass distribution of two photons before and after the correction. The peak

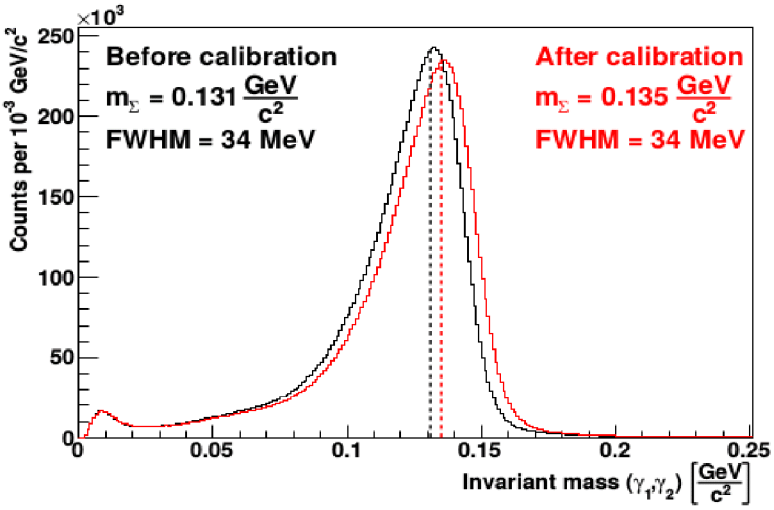

Figure 3.4. Invariant mass distribution of two photons. The dashed lines represent the peak position of the distribution before (black) and after (red) the calibration [39].

position is determined by fitting the invariant mass distribution with the Novosibirsk function [40].

$$f(x) = A\ exp\left[-0.5\left(\frac{log(1+\Lambda(x-x_0))}{\tau} \right)^2 + \tau^2 \right] \tag{3.5}$$

Here, Λ is defined as follows:

$$\Lambda = \frac{sinh(\tau\sqrt{log(4)})}{\sigma\sqrt{log(4)}} \tag{3.6}$$

In above equations, x_0 is peak position, σ is the resolution and τ describe the asymmetry in the Gaussian.

3.2.4 Track assignment

The hits in PSB and SEC are grouped into clusters and for MDC tracklet information is extracted. To determine whether a track is neutral or charged in nature, different sub-detector combinations are investigated. All combinations are examined by track reconstruction algorithm. The ge-

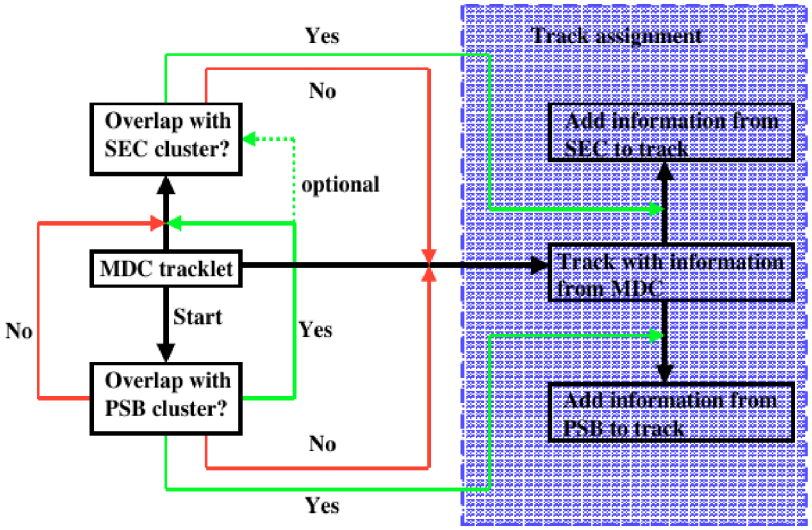

Figure 3.5. Schematic diagram of the track assignment in the Central Detector [39].

ometrical and time overlap is checked for the information of different hits

in individual detectors belong to one track. First, the traklets in MDC are examined for the overlap with PSB or SEC or both. If it does not coincide with any of them, then track is a charged track but contains the MDC information only. If the tracklets in MDC coincide with the clusters of PSB, the algorithm search for the cluster in SEC. If the combination is found, then the track is assigned as a charged track. The PSB clusters are checked for overlap with MDC and SEC, if the overlap is found with SEC only, then the track was not detected in the MDC. The tracks have clusters in SEC only without overlap with MDC and PSB are assigned as neutral tracks. The schematic depiction of tracks assignment procedure is shown in the Figure 3.5 and all possible combinations are summarized in the Table 3.1.

Detector combination	**Track type**
MDC, PSB, SEC	Charged, punching through SEC
MDC, PSB	Charged, stopped in PSB or solenoid
MDC, SEC	Charged, punching through SEC, without being detected in PSB
PSB, SEC	Charged, punching through SEC, without being detected in MDC
MDC	Charged, stopped in MDC
PSB	Charged, stopped in PSB or solenoid, without being detected in MDC
SEC	Neutral, detected in SEC only

Table 3.1. List of possible combinations of hits in the sub-detectors.

Chapter 4

Data Analysis

The aim of this work is to determine the electromagnetic transition form factor of the η meson through the study of it's Dalitz decay $\eta \rightarrow \gamma e^+e^-$. The η meson is produced in the proton-proton reaction at 1.4 GeV beam kinetic energy (excess of approximately 60 MeV) and the production cross section of pp$\rightarrow$ppη reaction at this energy is 9.8$\pm$1 μb [44]. In the analysis, η mesons are tagged by reconstructing all the final state particles of the pp$\rightarrow$ppη $\rightarrow$pp$e^+e^-\gamma$ reaction. The final state protons are reconstructed in the forward detector and the decay fragments of the η mesons e.g. e^+, e^- and γ are reconstructed in the central detector. Various kinematic conditions and background subtraction techniques are implemented in order to extract a clean sample of $\eta \rightarrow \gamma e^+e^-$. Analysis is mainly based on the monitoring of invariant mass or missing mass spectra of a set of particles. The invariant mass (IM) and the missing mass (MM_{pp}) are given by Eq. 4.1 and Eq. 4.2 respectively. The transition form factor depends on the invariant mass of e^+e^- (IMe^+e^-), which is the experimental observable.

$$IM = \sqrt{\left(\sum_{i=1}^{n} E_i\right)^2 - \left(\sum_{i=1}^{n} \vec{p_i}\right)^2} \tag{4.1}$$

$$MM_{pp} = \sqrt{\left(E_{beam} + E_{target} - \sum_{i=1}^{n} E_i\right)^2 - \left(\vec{p}_{beam} + \vec{p}_{target} - \sum_{i=1}^{n} \vec{p_i}\right)^2} \tag{4.2}$$

Where, Ei and $\vec{p_i}$ are the energy and three momentum vector of different particles. The E_{beam} and $\vec{p}_{beam}$ are energy and three momentum vector of the incoming proton beam, whereas, E_{target} and $\vec{p}_{target}$ are the energy and

three momentum vector of the target.

4.1 Presort

The data used for this study were aquired by the WASA detector setup for 7 weeks and saved in data run files. Each file has a size of roughly 21 GB per data run and total data size is 98 TB [39], which is basically known as the raw data. Major part of the data are multipion events which is a background for pp→ppη →pp$e^+e^-\gamma$ reaction. The analysis time can easily be reduced by performing a presort to the data. Presort is a procedure where selection conditions are implemented on raw data in order to reduce both the space taken by data on hard disc and the time needed for the analysis. Presort conditions are taken from reference [39]. The presort conditions implemented in this analysis are as follows:

- At least one pair of reconstructed protons with missing mass larger than 0.4 GeV/c^2 in the forward detector. This cut is influenced by simulation study which shows that the events with more than two proton tracks gives missing masses smaller than 0.4 GeV/c^2.
- At least one pair of oppositely charged tracks in the central detector because events with one pair has largest multiplicity.

The file has been reduced to a size of 1.9 GB per data run compared to 21 GB raw data file after passing through the presort conditions.

4.2 Experimental trigger

The trigger conditions implemented in the analysis are as follows:

- At least two hits in the second layer of the Forward Range Hodoscope including the condition that the FRH should have geometrical overlap with other forward tracking detectors as well.

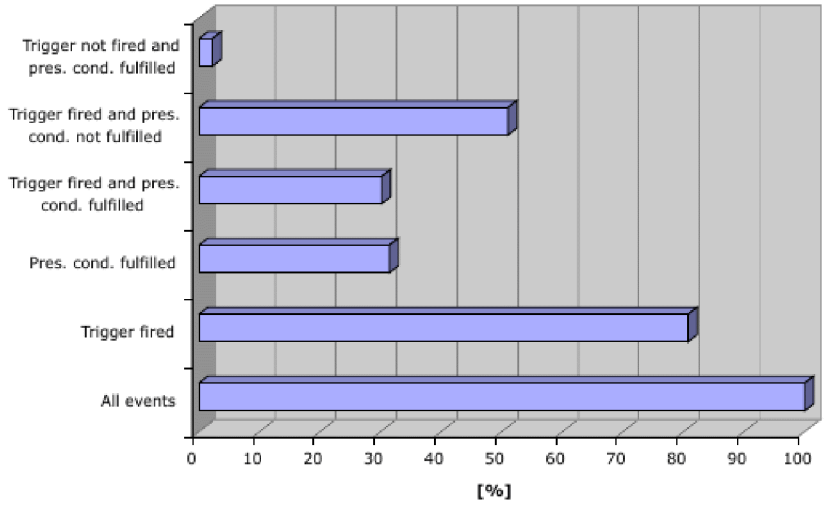

Figure 4.1. Trigger statistics.

- At least two hits in the PSB and at least one hit in the calorimeter are demanded.

The PSB hits take care of charged particles in the central detector and the calorimeter hits assure neutral hit in the central detector. A detail study of triggers have been done in reference [39] to finalize these trigger conditions. In the study, it is also observed that there is a 96% overlap between the presort conditions and the experimental trigger as shown in the Figure 4.1 (the figure is taken from [39]). It is not essential to request trigger during data analysis after presort. The histogram is filled when both the trigger and preselection condition are satisfied simultaneously for that event.

4.3 Identification of final state particles

4.3.1 Identification of protons

The protons are identified in the forward detector by means of their energy deposited in the FRH which has five layers (FRH1, FRH2, FRH3, FRH4 and FRH5). The Energy deposited by a charged track in the layers of FRH are compared as shown in the Figure 4.2. Solid black lines indicate

a region defined for the proton band. A charged track is identified as a proton when it lies within the proton bands in all plots. The ideal energy

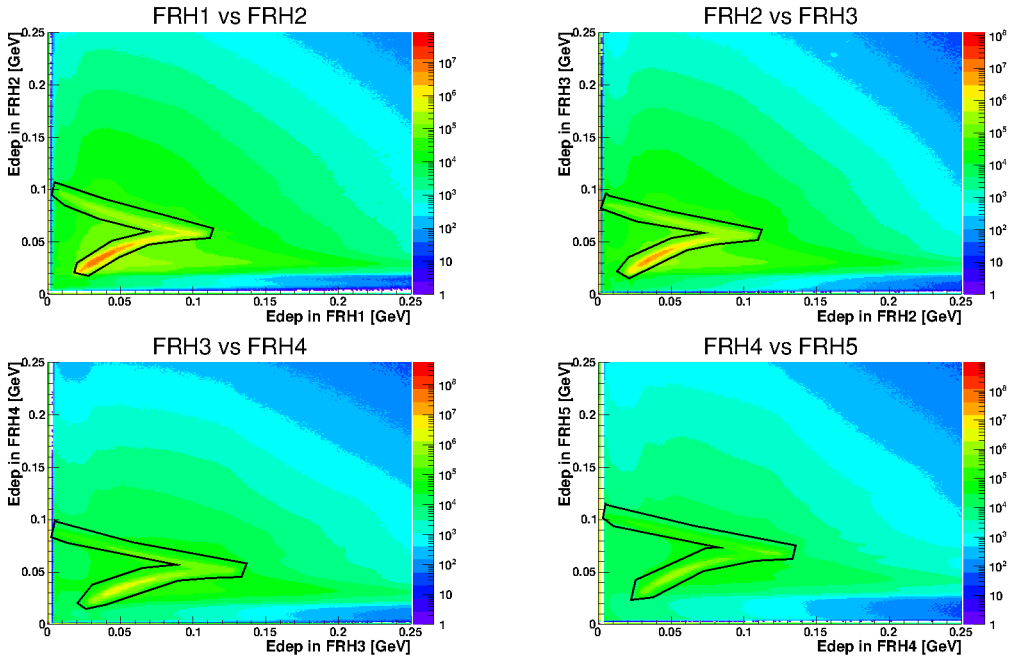

Figure 4.2. Energy deposited by charged tracks in FRH1 vs FEH2 **Top left)**,FRH2 vs FRH3 **Top right**, FRH3 vs FRH4 **Bottom left**, FRH4 vs FRH5 **Bottom right**. Solid black lines in indicate a graphical region to select protons.

deposite band for protons can be calculated using Bethe Bloch equation. A graphical region is defined around an ideal energy deposite band. The distance of the deposited energy is calculated from the ideal energy deposite band. This distance has been in a way that the proton candidates which are outside the solid black lines are removed. The proton selection procedure is taken from Daniel Lersch Thesis [39].

4.3.2 Identification of electrons

The identification of the charged particles in the central detector targets at selection of e^+ and e tracks. For the identification of electrons, momentum (P) information from the MDC and deposited energy (ΔE) from the SEC is utilized and ΔE-P method is used. The simulation studies indicate the location of electrons in ΔE-P plot in Figure 4.4. As evident from Figure 4.3, which is a plot from experimental data, the electron bands are shaded

with other stuff, which is certainly background for channel $\eta \to e^+e^-\gamma$. The Figure 4.5 shows the possible location of pions from $\eta \to \pi^+\pi^-\gamma$ decays, this is distribution from simulated $\eta \to \pi^+\pi^-\gamma$ data. The pions are majorly produced in both proton-proton reaction as well as in η meson decays. This is a challanging task to separate electrons from pions in this work. To reduce pion background, a linear cut shown in Figure 4.3, is taken from the simulation of the signal $\eta \to e^+e^-\gamma$ and is then, tuned for the data.

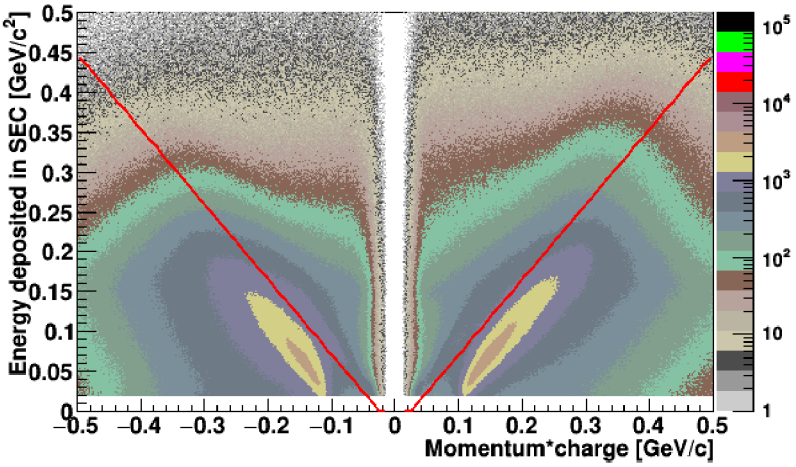

Figure 4.3. Momentum from MDC*charge vs Energy deposited in SEC for data

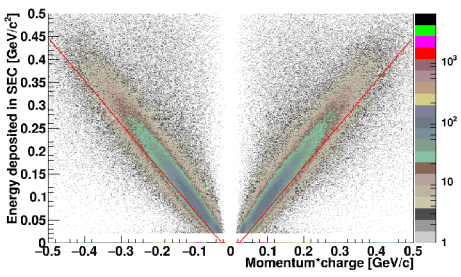

Figure 4.4. Momentum*charge vs Energy deposited in SEC for signal $\eta \to e^+e^-\gamma$ Monte Carlo simulation

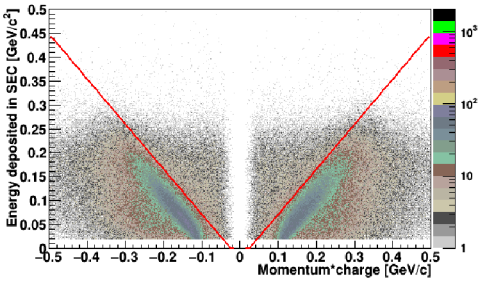

Figure 4.5. Momentum*charge vs Energy deposited in SEC for $\eta \to \pi^+\pi^-\gamma$ Monte Carlo simulation

4.3.3 Time coincidences in Forward and Central detector

The time coincidence conditions are implemented in the forward and central detector in order to select the tracks of the same event. The time information of the proton tracks are provided by the Forward Trigger Hodoscope. The time difference between two protons are checked after the selection of a pair of a proton. The distribution of the difference of the time between two proton tracks is shown in the Figure 4.6. Proton pairs with a time difference of 6 ns are selected for the further analysis.

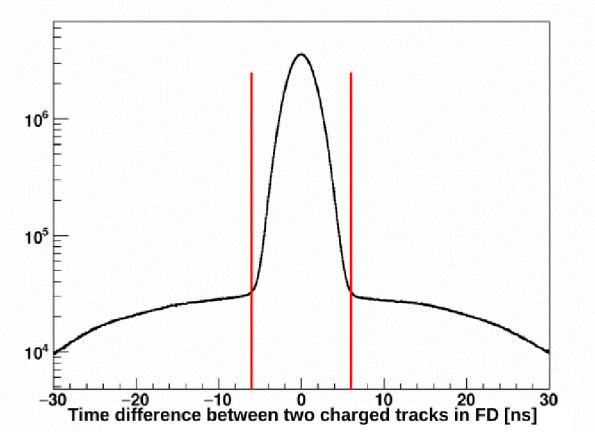

Figure 4.6. Time difference between two reconstructed proton tracks. The red lines indicate the time window of 6 ns or the selection of proton tracks.

The time information for the charged tracks in the central detector is provided by the PSB or SEC and the time information for neutral tracks are provided by SEC. The avarage proton time (t_{avg}) is calculated and then time difference between the t_{avg} and the time of charged (CDC) and neutral tracks (CDN) reconstructed in the central detector is examined in order to select a time window. The Figure 4.7 shows the correspoding time distributions. The time distributions in Figure 4.7 does not have a center at zero, because the time response functions of the detector where the time is measured are different. The time coincidence windows for the track selection in the central detector are listed in the Table 4.1.

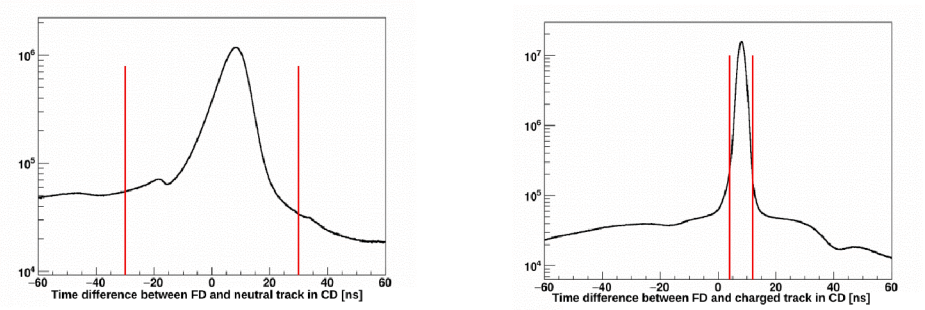

Figure 4.7. (a) Time difference between the t_{avg} and the time of neutral track in CD. (b) Time difference between the t_{avg} and the time of charged track in CD. The red lines indicate the time window for the further selection of the tracks in the central detector

Table 4.1. Time coincidence windows for track selection in the central detector.

FD-CDN time window (ns)	FD-CDC time window (ns)
-30 to 30	4 to 12

4.4 Basic Selection Criteria

In the $\eta \rightarrow e^+e^-\gamma$ decay, there are five particles (two protons, one electron, one positron and one photon) in the final state. The recoil protons are reconstructed in the forward detector, whereas, the decay fragents (e^+, e and γ) are reconstructed in the central tetector. The aim is to have a clean sample of $\eta \rightarrow e^+e^-\gamma$ decay. Following are the conditions to select the sample:

- All charged tracks are selected in the forward detector.
- Neutral tracks in CD within the time coincidense window with FD with minimum threshold energy 20 MeV.
- Charged tracks in CD within the time coincidense window with FD with minimum threshold energy 20 MeV.
- For the charged tracks, there should be atleast one hit in MDC and one hit in SEC.

4.5 Specific selection criteria for the channel

4.5.1 Energy momentum balance

The missing energy E_{miss} and missing momentum P_{miss} of the event is defined as follows:

$$E_{miss} = E_{target} + E_{beam} - (E_{p1} + E_{p2} + E_{e^+} + E_{e^-} + E_{\gamma}) \tag{4.3}$$

$$P_{miss} = P_{target} + P_{beam} - (P_{p1} + P_{p2} + P_{e^+} + P_{e^-} + P_{\gamma}) \tag{4.4}$$

Here, E_{target}, E_{beam}, E_{p1}, E_{p2}, E_{e^+}, E_{e^-}, E_{γ} stands for the energy for the target, beam and outgoing particles such as protons (p1 and p2), $e^{\pm}$ and γ respectively. Similarly, P_{target}, P_{beam}, P_{p1}, P_{p2}, P_{e^+}, P_{e^-}, P_{γ} stands for the momentum of the same particles. A detail study of E_{miss} and P_{miss} correlations of an event assist to understand the decay kinematics. The energy-momentum balance of the event is checked for the $\eta \to e^+e^-\gamma$ reaction hypothesis. The total missing energy and missing momentum of the system should be zero. The E_{miss}-P_{miss} distribution is shown in the Figure 4.8 for the experimental data. A cut on the values of E_{miss} and P_{miss} is implemented in order to reduce background. The events selected for further analysis steps have the E_{miss} greater than -0.2 GeV/c^2 but less than 0.2 GeV/c^2 and P_{miss} greater than 0.0 GeV/c but less than 0.2 GeV/c simulataneously. The conditions on the total missing energy and total missing momentum of the system are summaries as follows:

$-0.2 \leq$ Missing energy ≤ 0.2 && $0.0 \leq$ Missing momentum ≤ 0.2

This cut is influenced by simulation study. The E_{miss}-P_{miss} distribution shown in the Figure 4.9 is plotted from the simulated data for the signal channel $\eta \to e^+e^-\gamma$. In the simulation the entries are not located at zero due to the detector resolution and wrong reconstructions. This cut reduce the background substantially. However, it is seen in a simulation study of channel pp$\to$pp$\pi^0\pi^0$ that the pions are also located inside the box, as

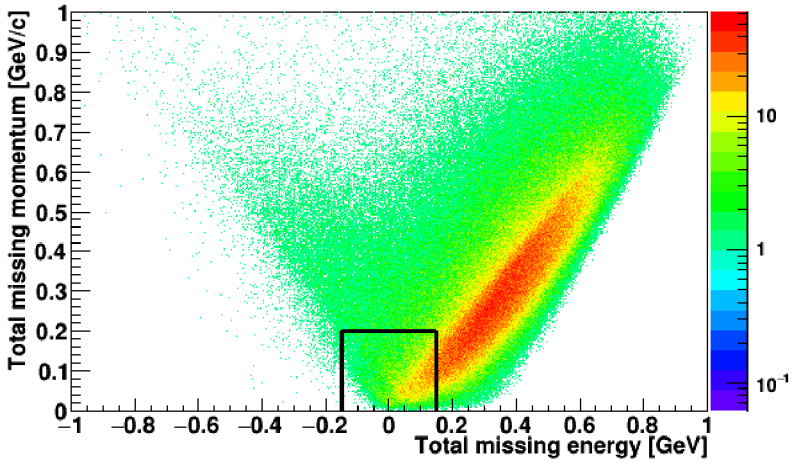

Figure 4.8. Total missing energy and total missing momentum of the system for the experimental data. The events within the box are selected for further analysis steps.

shown in the Figure 4.10. Further conditions are implemented on other kinematic variables in order to reduce the background.

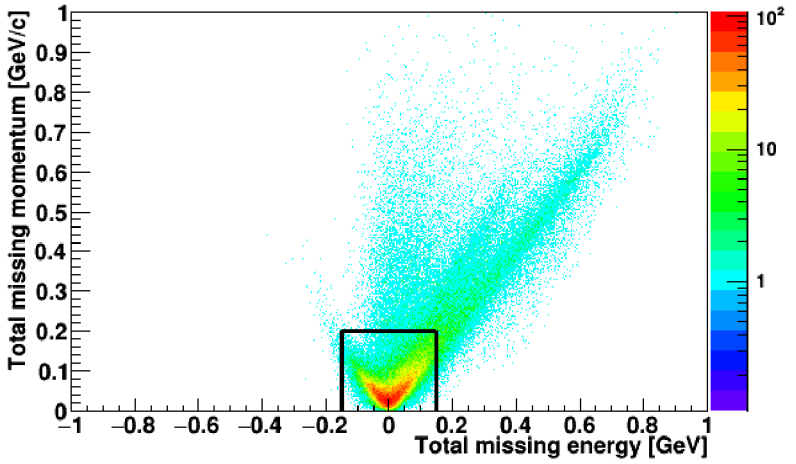

Figure 4.9. Total missing energy and total missing momentum of the system from simulated data for the signal channel $\eta \to e^+e^-\gamma$.

4.5.2 Conversion photons

In this study, it is crucial to distinguish the e^+e pairs originating from the primary interaction vertex from those originating from a secondary vertex. The beam pipe surrounds the interaction vertex. Therefore, when a photon

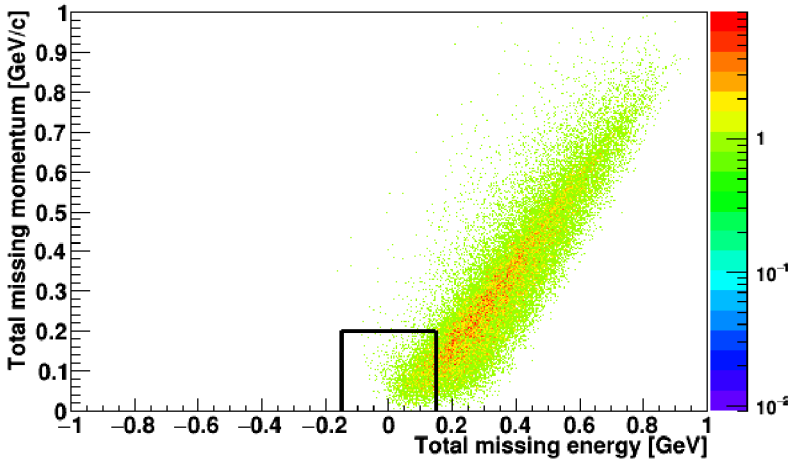

Figure 4.10. Total missing energy and total missing momentum of the system from simulated data for the a possible background channel $\eta \to \pi^0\pi^0$.

passes through the beam pipe, it can convert into a e^+e^- pair, which is known as photon conversion. The electrons from the signal $\eta \to e^+e^-\gamma$ originate from the primary vertex or origin. Hence, these electron's four-momentum vectors at the beam pipe has a non-zero opening angle between them, whereas, e^+e pair originated at the beam pipe has an opening angle close to zero (see Figure 4.11). In order to supress conversion photon background, the distribution of radius of the e^+e^- vertex in the xy-plane is plotted as a function of the invariant mass of the e^+e^- at the beam pipe, as shown in Figure 4.12.

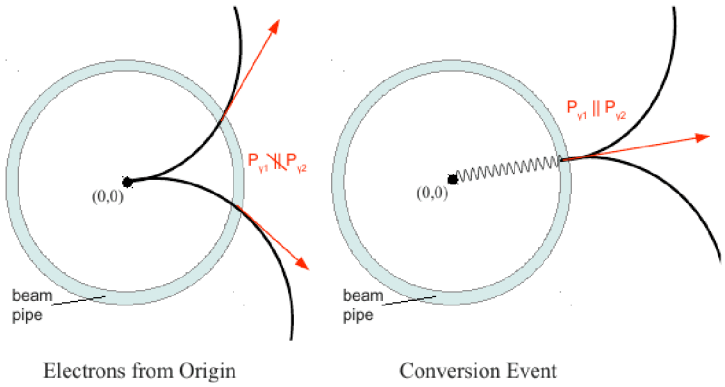

Figure 4.11. Schematic depiction of a non-conversion and conversion event. **LHS** shows non-conversion event, hence, a e^+e^- pair coming from the vertex. Here, the corresponding four vectors of the elctron pair have changed direction under the influence of magnetic field. **RHS** shows a conversion event, where electron pairs have originated from the beam pipe.

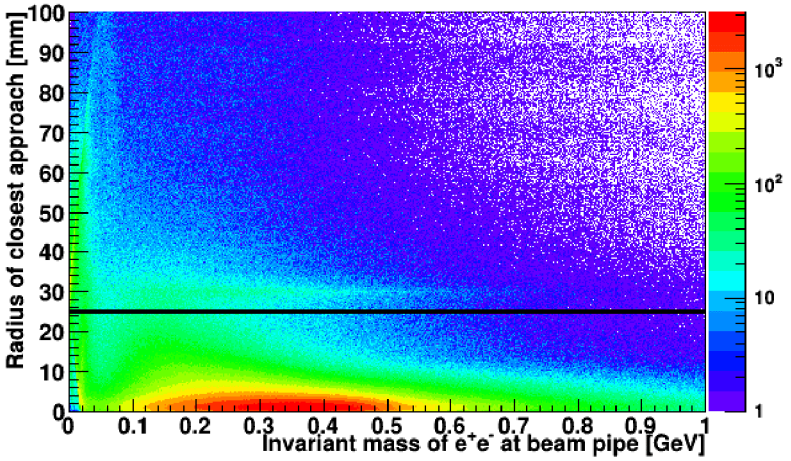

Figure 4.12. Invariant mass of e^+e^- at beam pipe vs Radius of closest approach from the experimental data.

The radius of the e^+e^- vertex in the x-y plane should be near to zero for the e^+e^- originating at primary vertex. However, this should be near 30 mm for the e^+e^- pairs originating at beam pipe as the radius of the beam pipe is 30 mm. The invariant mass of the e^+e^- at the beam pipe is for the pairs from primary vertex will be larger than those originate at beam, because they have a large opening angle. The momentum vectors

corresponding to the pairs originating at the beam pipe will be parallel, hence, the invariant mass will be approximetly twice of the electron mass. Figure 4.13 and 4.14 are from the simulation study of signal $\eta \to e^+e^-\gamma$ decays and $\eta \to \gamma\gamma$ decays.

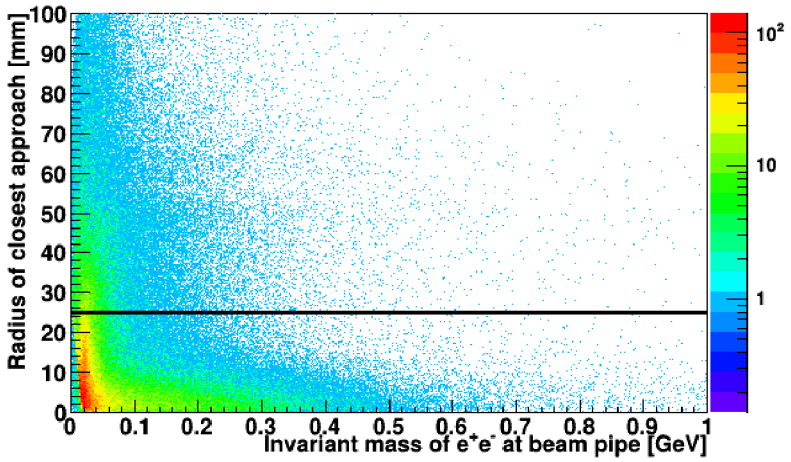

Figure 4.13. Invariant mass of e^+e^- at beam pipe vs Radius of closest approach for $\eta \to \gamma e^+e^-$ Monte Carlo simulation

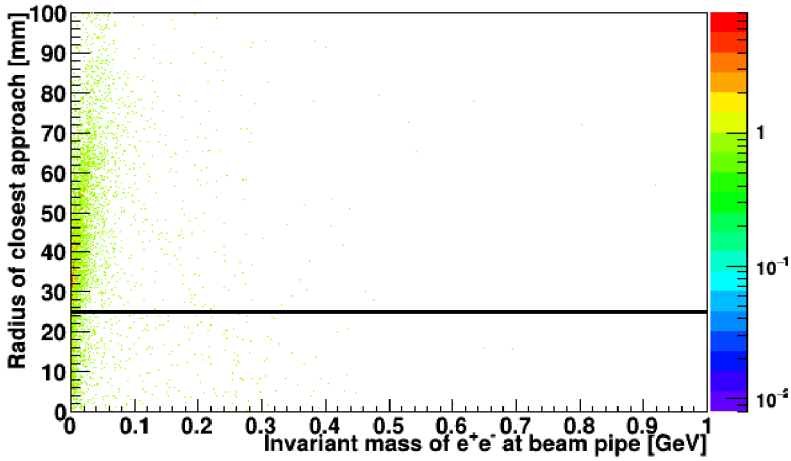

Figure 4.14. Invariant mass of e^+e^- at beam pipe vs Radius of closest approach for $\eta \to \gamma\gamma$ Monte Carlo simulation

In the $\eta \to \gamma\gamma$ decay, one of the photons interacts with the beampipe material and converts into e^+e^- pair and produce conversion background.

A separation between the conversion and non-conversion events near to the radius of beam pipe is clearly visible in the simulation studies as well. Events with position of radius of e^+e^- vertex above 28mm are rejected as those events contain conversion photons.

4.5.3 Split-offs

When a particle hit the calorimeter, it produces electromagnetic shower on the calorimeter crystals. In case on a continuous shower, the clustering algorithm will identify one cluster, however, the discontinuous shower will identify more than one cluster. The background present due to discontinuous electromagnetic shower in the calorimeter caused by a particle is called split-off. The energy deposited in the calorimeter is plotted as a function of the angle between a cluster and closest charged track as shown in the Figure 4.15.

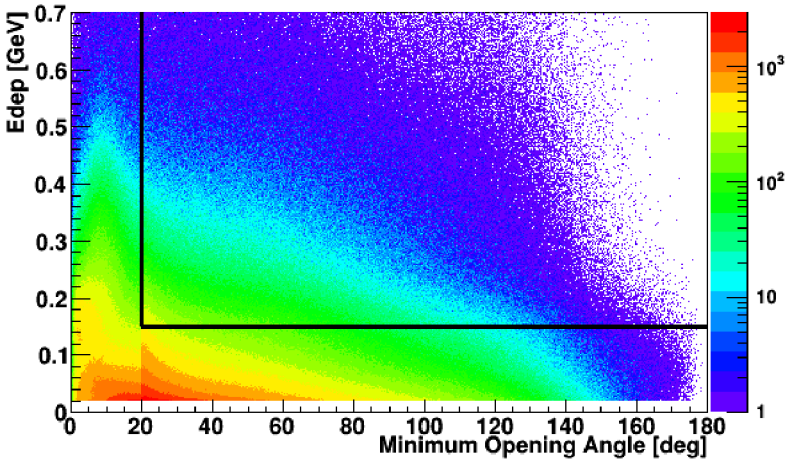

Figure 4.15. Deposited energy of reconstructed photons as a function of the minimum opening angle between a reconstructed calorimeter cluster and the closest charged track entering the calorimeter for experimental data

.

The simulation study shows that the split-off events are located at

small energy values and small angles. This is evident from Figure 4.16 and Figure 4.17. The events above the horizontal line and to the right hand side of the vertical line in Figure 4.15 are selected for the further analysis. This cut is influenced by simulation which is applied to reject split-offs.

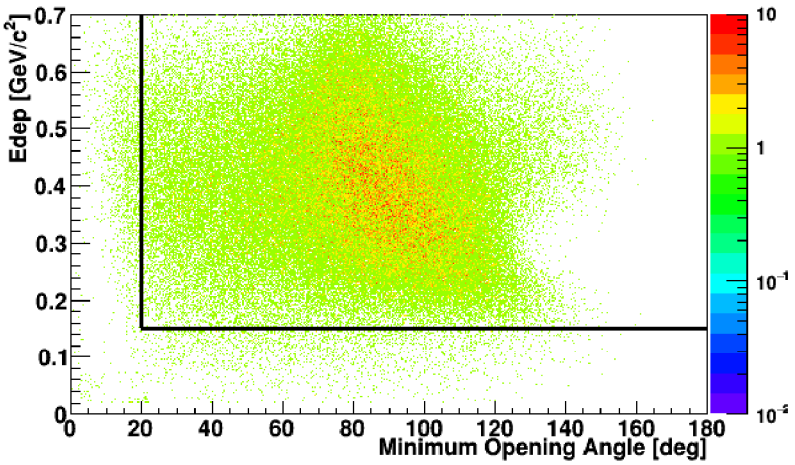

Figure 4.16. Deposited energy of reconstructed photons as a function of the minimum opening angle between a reconstructed calorimeter cluster and the closest charged track entering the calorimeter for $\eta \to \gamma e^+ e^-$ Monte Carlo simulation

.

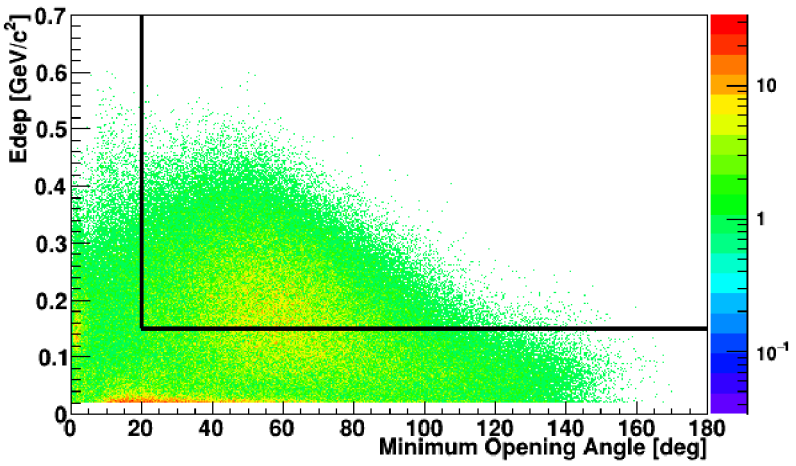

Figure 4.17. Deposited energy of reconstructed photons as a function of the minimum opening angle between a reconstructed calorimeter cluster and the closest charged track entering the calorimeter for $\eta \rightarrow \gamma\pi^+\pi^-$ Monte Carlo simulation

.

4.6 Background study

A detailed study is performed in order to identify different sources of the background. The direct pions produced in the proton-proton reaction contribute in available phase space and other η decays having larger cross-section and branching ratio contribute inside the peak region. It is essential to understand the source of background in order to extract a clean sample of $\eta \rightarrow e^+e^-\gamma$ events. All possible sources of the background have been studied. The pp$\rightarrow$pp$\pi^0\pi^0$ reaction has large cross-section (324 μb) at 1.4 GeV. In this reaction, when one pion does a Dalitz decay and two photons are failed to register in the calorimeter, it mimics the signal channel. Hence, it could pass the selection criteria. With a larger cross-section compare to pp$\rightarrow$ppη reaction, the pp$\rightarrow$pp$\pi^+\pi^-\pi^0$ can also pass through the selection criteria as this reaction has a similar topology as the signal channel. The channel $\eta \rightarrow \gamma\gamma$ contributes as a background if one of the photons interact with the beampipe material and converts into $e^{\pm}$ pair. Both $\eta \rightarrow \gamma\pi^+\pi^-$

and $\eta \rightarrow \pi^0\pi^+\pi^-$ channels have a similar topology to the signal channel as in both the channels there are two oppositely charged tracks and one neutral track. The cocktail has been plotted in order to see the background contribution in the experimental data. Figure 4.18 is the resultant cocktail plot. All the channels are simulated using Pluto event generator. All background distributions are normalized with the corresponding branching ratios, cross-section and relative to each other and then have been scaled with the data. The background channels are listed in Table 4.2, the third column of the table defines the secondary decays of π^0. The values of cross-section and branching ratios in the table are taken from the Particle Data Group [10]. It is evident from the Figure 4.18 that pp→pp$\pi^0\pi^0$ is the

Table 4.2. List of simulated background channels.

Channel	Cross-section / Branching ratio	π^0 decay
$pp \rightarrow pp\pi^0\pi^0$	324 μb	$\pi^0(e^+e^-\gamma)\pi^0(\gamma\gamma)$
$pp \rightarrow pp\pi^+\pi^-\pi^0$	4.6 μb	$\pi^0(e^+e^-\gamma)$
$pp \rightarrow pp\pi^0\pi^0\pi^0$	1.34 μb	$\pi^0(e^+e^-\gamma)\pi^0(\gamma\gamma)\pi^0(\gamma\gamma)$
$\eta \rightarrow \pi^+\pi^-\pi^0$	22.6%	-
$\eta \rightarrow \pi^+\pi^-\gamma$	4.68%	-
$\eta \rightarrow \gamma\gamma$	39%	-
$\eta \rightarrow \pi^0\pi^0\pi^0$	32%	$\pi^0(e^+e^-\gamma)\pi^0(\gamma\gamma)\pi^0(\gamma\gamma)$

main source of the background in the phase space region. The simulation study shows that the $\eta \rightarrow \gamma\gamma$ is the main source of background inside the peak region, it contributes 6.21 % inside the peak region. A total of 7.6% background contributes from the η decay channels $\eta \rightarrow \gamma\gamma$, $\eta \rightarrow \gamma\pi^+\pi^-$, and $\eta \rightarrow \pi^0\pi^+\pi^-$ inside the peak region. The contributions are summarize in the Table 4.3 and shown in the missing mass distribution in Figure 4.19.

Table 4.3. List of simulated in-peak background channels.

Channel	Background contribution (%)
$\eta \rightarrow \gamma\gamma$	6.21
$\eta \rightarrow \pi^+\pi^-\pi^0$	0.78
$\eta \rightarrow \pi^+\pi^-\gamma$	0.64

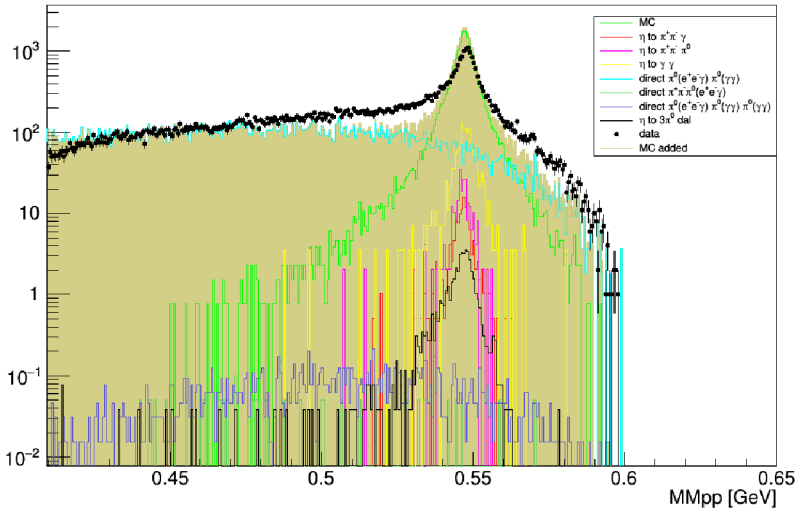

Figure 4.18. Cocktail plot of missing mass including experimental data after passing through the selection conditions.

4.7 Missing mass for pp→ppη reaction

The two proton missing mass distribution is shown in the Figure 4.20 after implementing all kinematic conditions and background subtraction methods. It is evident from the missing mass distribution that η peak is sitting over a phase space background. This background mainly comes from direct pion production in the proton-proton reaction. The missing mass distribution is fitted with a sum of fourth order polynomial multiplied with the simulated background ($pp \to pp\pi^0\pi^0$) and simulated signal $\eta \to \gamma e^+e^-$ in order to remove the phase space background. Finally, 33k $\eta \to e^+e^-\gamma$ events are reconstructed. However, these events contain in-peak background from $\eta \to \gamma\gamma$, $\eta \to \gamma\pi^+\pi^-$, and $\eta \to \pi^0\pi^+\pi^-$ decays.

The transition form factor of the η meson is calculated using these events. The method to obtain the form factor has been discussed in detail in the next chapter.

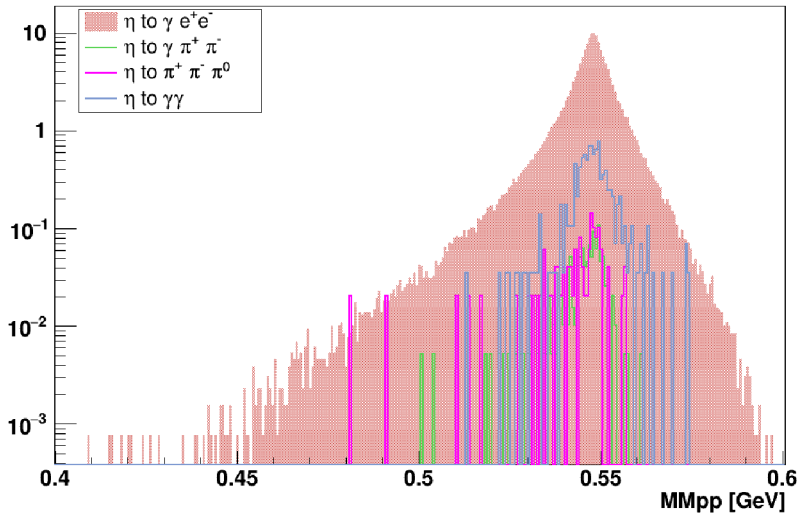

Figure 4.19. Montecarlo cocktail plot of missing mass after passing through the selection conditions.

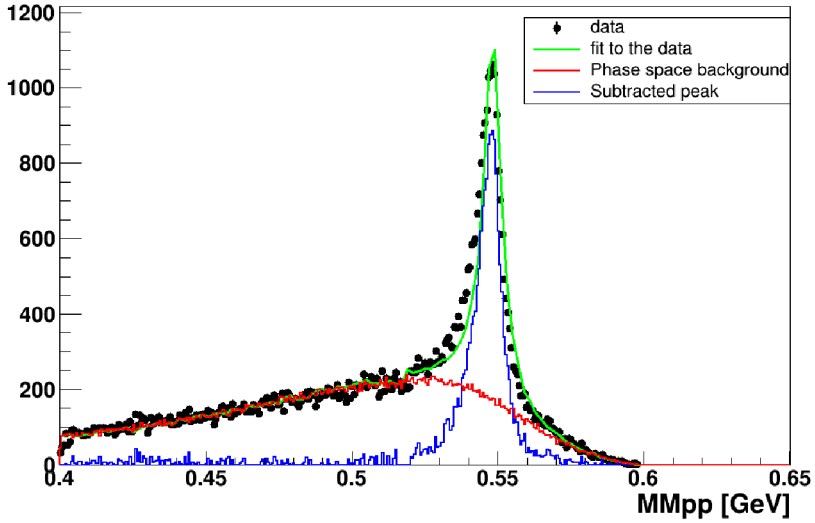

Figure 4.20. Missing mass of incoming and outgoing protons for pp→ppη reaction after passing through all selectiom conditions discussed. Black are the data points, green line represent a global fit to the data, red line represent the background and blue line is the resultant missing mass distribution after the background subtraction

Chapter 5

Result and Discussion

5.1 Calculation of the Transition Form Factor

A 2D histogram of missing mass of protons (MM_{pp}) for the reaction pp→ppη as a function of the invariant mass of e^+e^- ($IM_{e^+e^-}$) is shown in the Figure 5.1.

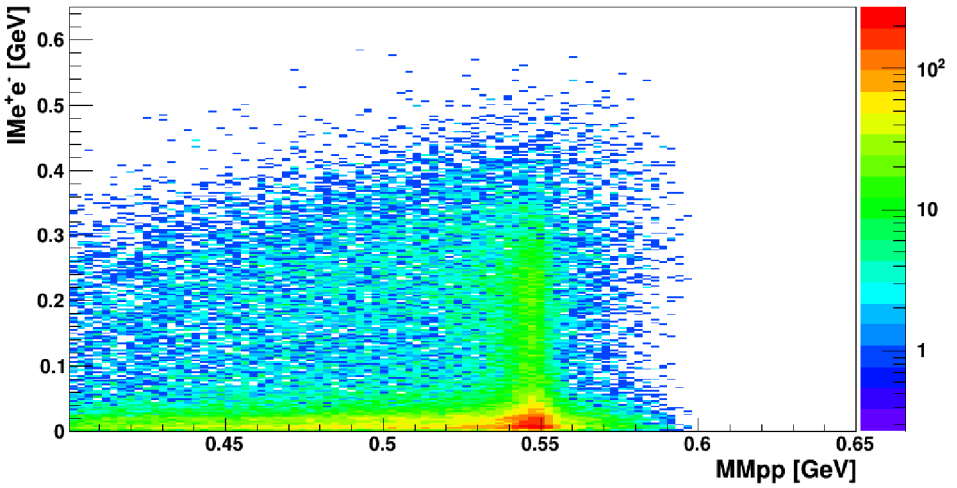

Figure 5.1. Experimental distribution of the missing mass as a function of the invariant mass of the e^+e pair after applying event selection described in previous chapters.

The missing mass for the pp→ppη reaction is determined for each 52 MeV $IM_{e^+e^-}$ interval separately by taking a projection of 52 MeV in $IM_{e^+e^-}$

axis. The projections are shown in the Figure 5.2.

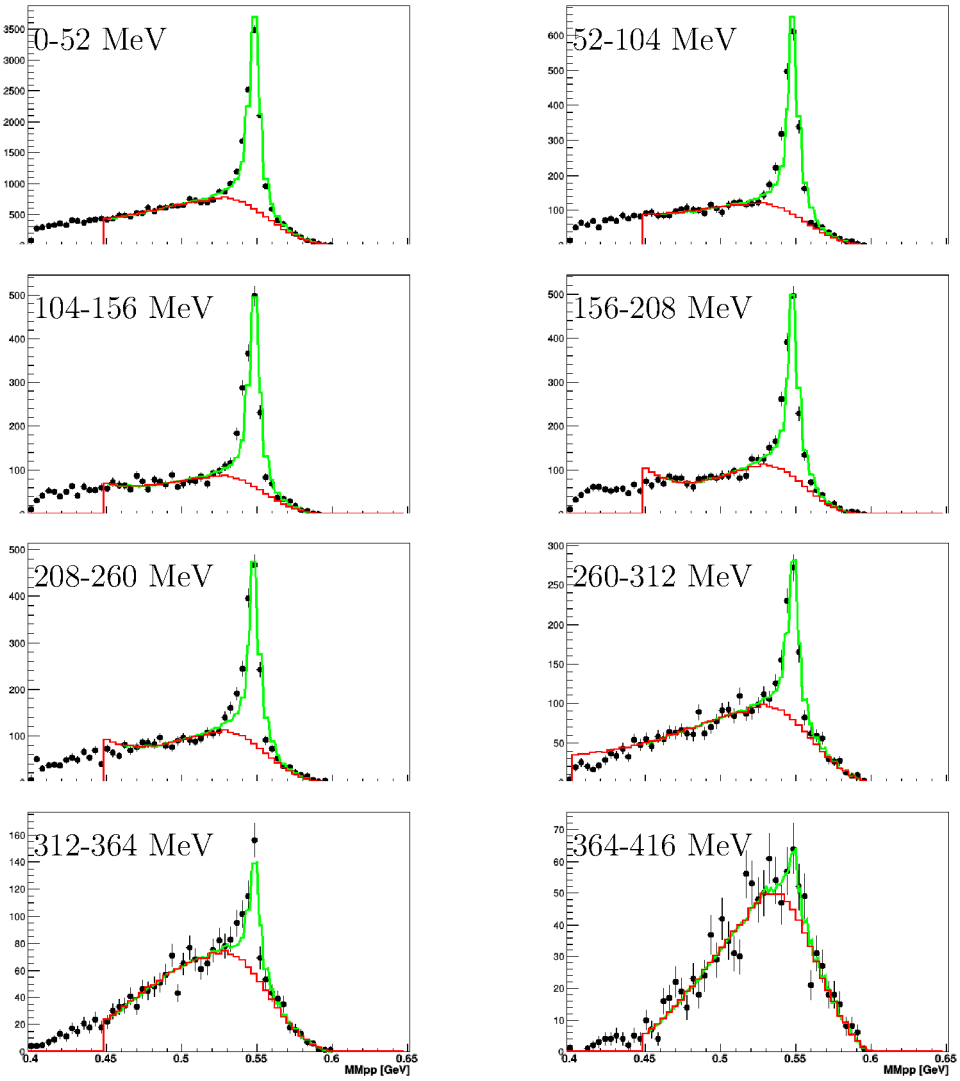

Figure 5.2. Missing mass distribution for each $IM_{e^+e^-}$ intervals. Green lines are a global fit to data and red lines shows the background extracted from the global fit.

Each missing mass distribution is fitted with a sum of polynomial multiplied with a simulated $pp \to pp\pi^0\pi^0$ and simulated signal $\eta \to \gamma e^+e^-$ in order to subtract background. The simulated $pp \to pp\pi^0\pi^0$ is used because it mimics to the background shape. The fitting fuction is given as:

$$polX^*MC(pp \to pp\pi^0\pi^0) + MC(\eta \to \gamma e^+e^-) \tag{5.1}$$

Here, polX is a polynomial of order X. A 4^{th} order polynomial is used

for first three distributions and for remaining distribution a third order polynomial is used. MC stands for Monte Carlo simulation. Then, the signal is extracted for each $IM_{e^+e^-}$ interval. The signal content is calculated by integrating the distribution in 535-565 MeV window after subtracting the phase space background. A background subtracted invariant mass is shown in the Figure 5.3.

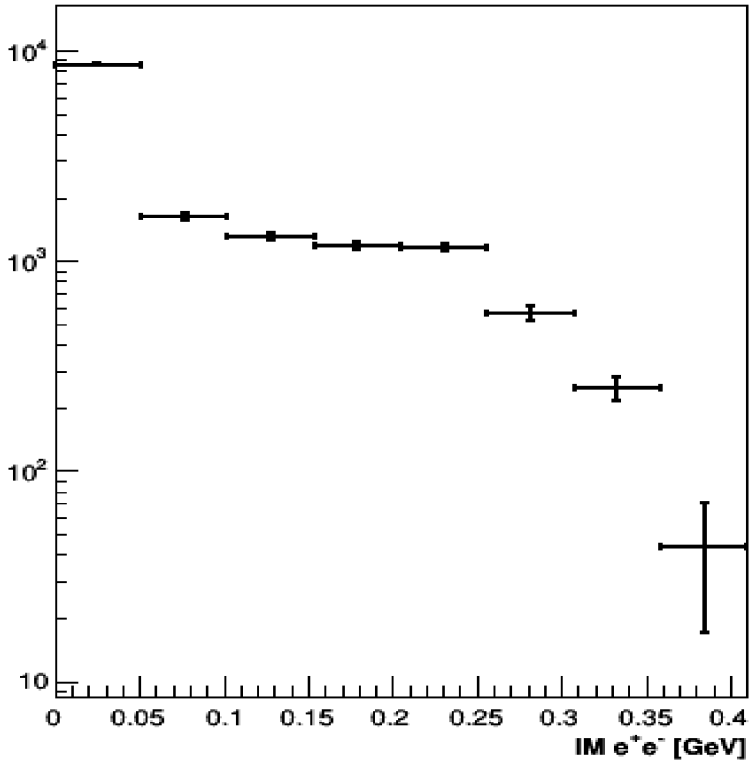

Figure 5.3. Invariant mass distribution of e^+e^- after the background subtraction.

The background subtracted invariant mass distribution is then compared with sum of simulated signal and possible backgrounds ($\eta \to \gamma\gamma$, $\eta \to \pi^+\pi^-\gamma$, $\eta \to \pi^+\pi^-\pi^0$). It is seen in the Figure 5.4 that the data does-not agree with simulation. A detailed study in order to understand the background has been discussed in previous chapter. All possible physical backgrounds have been checked.

Then, experimental data points are divided by the Monte Carlo data using QED to obtain the transition form factor. To obtain the invariant

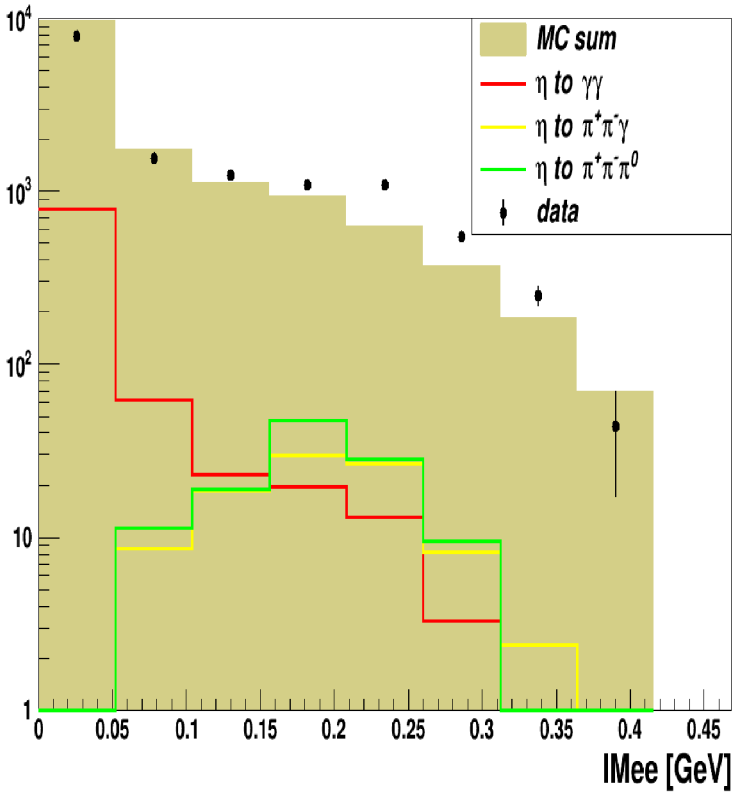

Figure 5.4. Comparison of experimental invariant mass distribution of e^+e^- with simulation.

e^+e^- using QED, 1M $\eta \to e^+e^-\gamma$ events are simulated according to QED using PLUTO event generator and analysed. The data points using QED are plotted with experimental data in Figure 5.5. The QED spectrum is normalized to the experimental data. Figure 5.6 shows the resulting form factor $|F(q^2)|^2$ distribution with statistical uncertainties. Some of the Form Factor bins show fluctuations. These fluctuations are the result of disagreement between data and simulation and attributed to some unknown source of background which has yet to be understood. If the fluctuations are neglected, hence the $|F(q^2)|^2$ as a fuction of IMe^+e^- is plotted from the Monte Carlo sum in the Figure 5.4, the form factor can be reproduced without fluctuations. The resulting distribution is shown in the Figure 5.7.

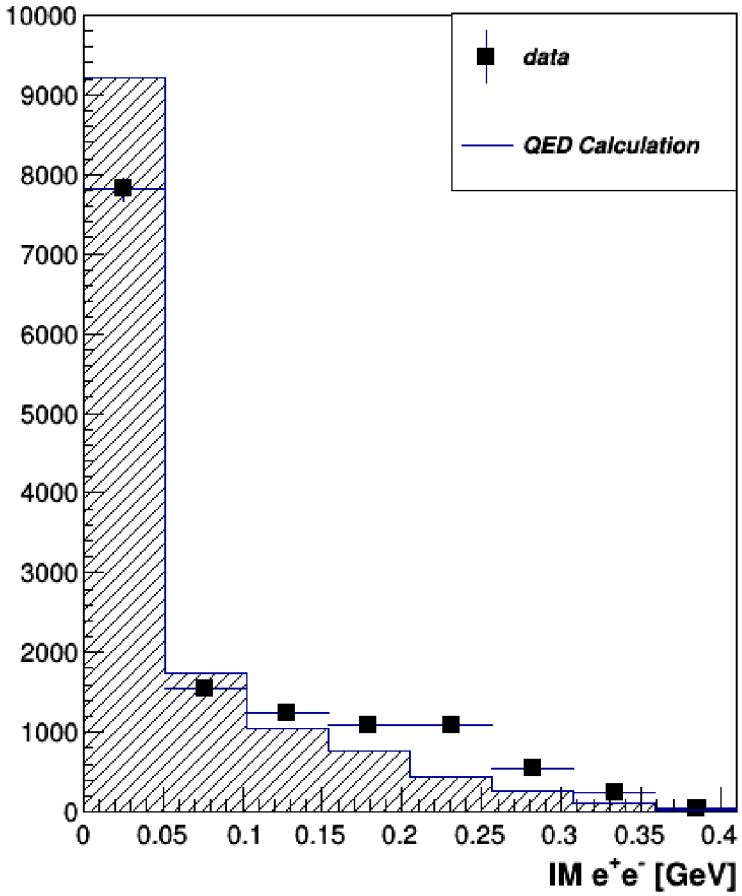

Figure 5.5. Experimental invariant mass distribution of e^+e^- after the background subtraction. Filled histogram corresponds to the simulated data using QED.

Then, the form factor distribution Figure 5.6 is fitted with the single-pole formula, given in the Equation 5.2

$$[F(q^2)]^2 = \left[\alpha\left(1 - \frac{q^2}{\Lambda_P^2}\right)\right]^2 \tag{5.2}$$

Here, α is a normalization paremeter, $q^2 = IM_{e^+e^-}$ is the mometum transfer which is equal to the invariant mass of e^+e^- and Λ^{-2} is the slope parameter, which is extracted from the fit. Although the χ^2/ndf is very large (29.2) due to the fluctuations.

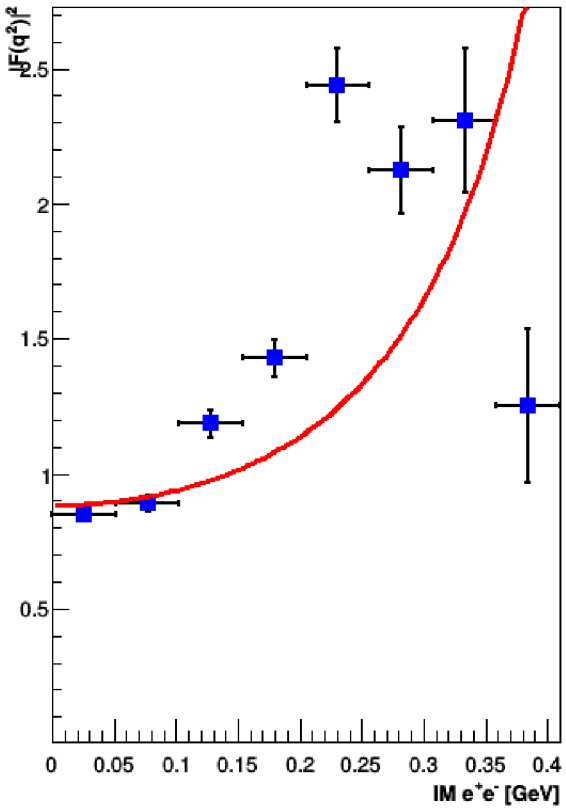

Figure 5.6. The form factor $|F(q^2)|^2$ as a function of IM e^+e^-. Red line is the fit to the data points. The error bars are statistical.

The value of the the slope parameter Λ_P^{-2} amounts to $2.8 \pm .13$ GeV^{-2}.A comparision of the result from this work with other WASA measurement is summarised in the Table 5.1.

Table 5.1. Summary of the results from other WASA experiments.

Datasets	Slope parameter Λ_P^{-2} (GeV^{-2})
pdη 2008	$2.27 \pm 0.73_{stat}$
ppη 2008	$1.9 \pm 0.33_{stat}$
ppη 2012	$1.97 \pm 0.29_{stat} \pm^{0.13_{syst}}_{0.23_{syst}}$
ppη 2010 (this work)	$2.8 \pm 0.13_{stat}$

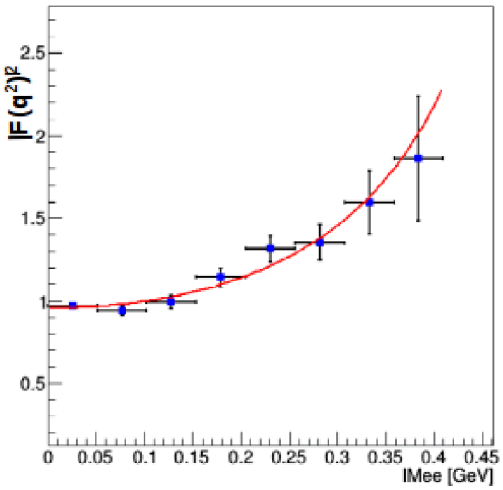

Figure 5.7. The form factor $|F(q^2)|^2$ as a function of IM e^+e^- from the simulation (Monte Carlo sum scaled with data). Red line is the fit to the data points. The error bars are statistical.

5.2 Estimation of the Systematic Uncertainty

The value of slope parameter, Λ_P^{-2}, varies by changing the kinematic conditions. The possible sources for the systetmatic uncertainty are listed as follows:

- Different kinematic conditions and methods used for the background subtraction such as linear cut for the identification of electrons, the energy-momentum balance cut, the cut on the radius of e^+e^- in order to supress the conversion background and split-off cut.
- The size of invariant mass of e^+e^- bin to subtract the background.
- The integration window to calculate the $\eta \to e^+e^-\gamma$ events.

In this study the invariant mass of e^+e^- bin and integration window to calculate the $\eta \to e^+e^-\gamma$ events has been taken into account. Different set

of the slope parameters, Λ_P^{-2} are obtained by varing the the bin size and integration window. Finally, the systematic uncertainty is calculated using the following formula:

$$\sigma_{sys} = \frac{1}{N}\sqrt{\Sigma(x_{ref} - x_i)} \tag{5.3}$$

Here, N is the number of measurements, x_{ref} is the reference value and x_i the value of the slope parameter for corresponding measurement. The values of slope parameters are listed for different measurements in the Table 5.2. The value of the systematic uncertainty calculated using Eq. 5.3 is:

Table 5.2. Slope parameter Λ_P^{-2} for a set of measurements.

Integration window (GeV)	Bin size (MeV/c^2)	Slope parameter Λ_P^{-2} (GeV^{-2})
530-565	26	2.9 $\pm$ 0.12
530-565	52	3.1 $\pm$ 0.12
535-565	26	2.4 $\pm$ 0.13
535-565	52	2.8 $\pm$ 0.13

$\sigma_{sys} = 0.16$ GeV^{-2} and the value of slope parameter is $\Lambda_P^{-2} = 2.8 \pm 0.13_{stat}$ $\pm$ 0.16_{sys} GeV^{-2}. Here, all possible sources of systematic effects have not been examined due to the time constrain, remaining checks will be done in further studies.

5.3 Summary and Outlook

A study of $\eta \to e^+e^-\gamma$ Dalitz decay has been done to extract the electromagnetic transition form factor of η meson. For this study, the experiment took place using WASA-at-COSY facility in Juelich, Germany and the data were aquired for 7 weeks in 2010. The η meson was produced in proton-proton reaction at beam energy 1.4 GeV. The recoil protons are identified in the forward part of the detector and the decay product of η mesons are identified in the central detector. The large cross-section of ppη raction allows studying rare decay process. However, it also contributes a large background from multi-pion production.

Various kinematic conditions and methods have been used to reduce the background. Approximately 33k $\eta \to e^+e^-\gamma$ events were reconstruced. Finally, with a clean sample of $\eta \to e^+e^-\gamma$, the η transition form factor was calculated as a function of the e^+e^- mass.

The value of the the slope parameter Λ_P^{-2} amounts to $2.8 \pm 0.13_{stat} \pm 0.16_{sys}$ GeV^{-2}. The statistical accuracy achieved in this work is least compared to previous measurements of WASA-at-COSY experiments. However, fluctuations are observed in few bins of form factor distribution. The reason for these fluctuations needs to be found which is in progess. A detailed study of systematic uncertainties on the value is in progress. In addition, kinematic fit to the data is also in progress, which will help to reduce the background. Later on, other ppη datasets can be combined with the analyzed data set of this work. This will result in an increase in the statistics which will further improve the result.

Bibliography

[1] [Image credit] url:https://sciencesprings.files.wordpress.com/2016/05/standard-model.jpg. xv, 2

[2] G. Aad et al. Observation of a new particle in the search for the Standard Model Higgs boson with the ATLAS detector at the LHC. Phys. Lett. , B716:1-29, 2012. doi: 10.1016/j.physletb.2012.08.020. 2

[3] S. Chatrchyan et al. Observation of a new boson at a mass of 125 GeV with the CMS experiment at the LHC. Phys. Lett. , B716:30-61, 2012. doi: 10.1016/j.physletb.2012.08.021. 2

[4] https://www.physics.umd.edu/courses/Phys741/xji/chapter1.pdf. Accessed 9 May 2018. 4

[5] L. G. Landsberg, Electromagnetic Decays of Light Mesons, Phys. Rept. 128, 301376 (1985). xv, 4, 8, 9, 10, 11

[6] Bethke S. (2000), Determination of the QCD Coupling α_s, J. Phys. G26, R27. xv, 4

[7] A. Pevsner and others, Evidence for a three pion resonance near 550 MeV, Phys. Rev. Lett. 7, 421-423 (1961). 5

[8] Wilczek F. (2000), QCD made simple, Phys. Today, doi:10.1063/1.1310117 5

[9] A. Bramon, R. Escribano, and M. D. Scadron. The $\eta - \eta^{'}\theta$ mixing angle revisited. Eur. Phys. J., C7:271278, 1999. 6

[10] C. Amsler et al. Review of particle physics. Phys. Lett., B667:1, 2008. xxi, 6, 60

[11] N. M. Kroll and W. Wada, Internal pair production associated with the emission of high-energy gamma rays, Phys. Rev. 98, 13551359 (1955). 8

[12] J. F. McGowan, An isobar model for $e^+e^- \to \pi^+\pi^-\pi^0\pi^0$, (1995) arXiv:9501399 [hep-ph]. 9

[13] L. Ametller, J. Bijnens, A. Bramon and F. Cornet, Transition form factors in π^0 , η and η and $\eta^{'}$ couplings to $\gamma\gamma$, Phys. Rev. D45, 986989 (1992). 11

[14] M. R. Jane and others, A Measurement of the Electromagnetic Form-Factor of the η Meson and of the Branching Ratio for the η Dalitz Decay, Phys. Lett. B59, 103 (1975). 12, 14

[15] R. Arnaldi and others, Study of the electromagnetic transition form-factors in $\eta \to \mu^+\mu-\gamma$ and $\omega \to \mu^+\mu^-\mu^0$ decays with NA60, Phys.Lett. B677, 260266 (2009). 12, 14

[16] A. Uras (for the NA60 Collaboration), Acta Phys. Pol. B 5, 465(2012). 12, 14

[17] R. I. Dzhelyadin and others, Investigation of η meson electromagnetic structure in $\eta \to e^+e^-\gamma$ decay, Phys. Lett. B94, 548 (1980). xv, 12, 14

[18] M. N. Achasov and others, Study of Conversion Decays $\phi \to \eta e^+e^-$ and $\eta \to e^+e^-\gamma$ in the Experiment with SND Detector at the VEPP-2M Collider, Phys. Lett. B504, 275281 (2001) 13, 14

[19] H. Berghauser, V. Metag, A. Starostin, P. Aguar-Bartolome, L. K. Akasoy and others, Determination of the eta-transition form factor in the $\gamma p \to p\eta \to p\gamma e^+e^-$ reaction, Phys. Lett. B701, 562567 (2011). 13, 14

[20] P. Aguar et al, New determination of the transition form factor in the Dalitz decay $\eta \to e^+e^-\gamma$ with the Crystal Ball/TAPS detectors

at the Mainz Microtron, PHYSICAL REVIEW C 89, 044608 (2014). 13, 14

[21] P. Adlarson et al. Measurement of the with the A2 setup at MAMI. $\omega \to \pi^0 e^+ e^-$ and $\eta \to \pi^0 e^+ e^-$ Dalitz decays, Phys. Rev. , C95(3):035208, 2017. doi: 10.1103/ PhysRevC.95.035208 14

[22] M. Hodana. Study of the $\eta \to \pi^0 e^+ e^-$ decay using WASA-at-COSY detector system . PhD thesis, Jagiellonian University, Cracow, 2012. 14

[23] H. Bhatt. Study of a rare decay $\eta \to \pi^0 e^+ e^-$ using WASA-at-COSY . PhD thesis, Department of Physics, Indian Institute of Technology, Bombay, 2011. 14

[24] D. Pszczel. Search for a new light boson in meson decay . PhD thesis, National Centre for Nuclear Research, Warsaw, Poland, 2017. 14

[25] Calen, H., Pellet Beam Dump modification. $WASA - at - COSYCollaborationWIKI - ID : Pelletdump_HC080107URL : http : //wasasrv.ikp.kfa - juelich.deWasaWiki/$ (January 2008). 17

[26] S. Kullander and P. Zielinski. . Uppsala Accelerator News, 4, 1987. 17

[27] H. H. Adam, Proposal for the Wide Angle Shower Apparatus (WASA) at COSY-Juelich - WASA at COSY (2004). 4, 17, 18

[28] Maier, R.: Cooler synchrotron COSY - performance and perspectives. Nuclear Instruments and Methods in Physics Research A, 390(1-2):18, May 1997. 17

[29] Brutigam, W. et al.: Status and perspectives of the cyclotron JULIC as COSY injector. NUKLEONIKA, 48:123126, 2003. 18

[30] R. Gebel, Maier R., and H. Stockhorst. Barrier-bucket RF tests. IKP COSY Annual Report 2008, Juelich-4282, 2009. 18

[31] Norman, G., Pellet Target Documentation. Internal document, (April 2004). xv, 20, 21

[32] H. H. Adam et al. Proposal for the Wide Angle Shower Apparatus (WASA) at COSY-Juelich - WASA at COSY. 2004. 20, 21, 22, 23, 24, 25, 26, 27, 28, 29, 30

[33] I. Frohlich et al. Pluto: A Monte Carlo Simulation Tool for Hadronic Physics. PoS ,ACAT2007:076, 2007. 32

[34] R. Schicker et al. Acceptance and resolution simulation studies for the dielectron spectrometer HADES at GSI. Nucl. Instrum. Meth. ,A380:586-596, 1996. doi:10.1016/0168-9002(96)00732-2. 32

[35] F. James, Monte-Carlo phase space, CERN 68-15 (1968). 32

[36] R. Brun, F. Bruyant, F. Carminati, S. Giani, M. Maire, A. McPherson, G. Patrick, and L. Urban. GEANT Detector Description and Simulation Tool. 1994. 33

[37] V. Hejny, M. Hartmann, and A. Mussgiller. Rootsorter, A New Analysis Framework for ANKE. Forschungszentrum Juelich Annual Report 2002. 33

[38] R. Brun and F. Rademakers. ROOT - An Object Oriented Data Analysis Framework. Nucl. Inst. Meth. in Phys. Res., $A389$: 8186, 1997. 33

[39] D. Lersch. Investigation of dipion final state interactions in $pp \to pp[\eta \to \pi^+\pi^-\gamma]$. Ph.D. thesis, Fachbereich fur Mathematik und Naturwissenschaften der Bergischen Universitat Wuppertal, 2014. xvii, 37, 41, 42, 46, 47, 48

[40] The CBELSA/TAPS Collaboration. In-medium mass from the $\gamma + Nb \to \pi^0\gamma + X$ reaction. Physics Review, C82:035209, 2010. 42

[41] K. A. Olive et al., Review of Particle Physics, Chin. Phys. C38 (2014) 090001 36

[42] C. Redmer, In search of the box anomaly with the WASA facility at COSY , PhD thesis, Bergische Universitat Wuppertal, 2010. 37

[43] W. R. Leo, Techniques for nuclear and particle physics experiments, Springer-Verlag, 1994.

[44] The CELSIUS/WASA Collaboration. The pp→pp$\pi\pi\pi$ reaction channels in the threshold region. Physics Letters, B649:122127, 2007. 45

[45] C. Terschlusen and S. Leupold. Electromagnetic transition form factors of light vector mesons. Phys. Lett. , B691:191-201, 2010. doi: 10.1016/j.physletb.2010.06.033.

[46] Prasuhn, D. et al.: Electron and stochastic cooling at COSY. Nuclear Instruments and Methods in Physics Research A, 441(1-2):167174, February 2000.